chemical-induced carcinogenesis model was chosen in the present study. DMBA and TPA enabled us to produce papillomas within 1–2 months. Furthermore, the number of chemical-induced papillomas was much more than that induced by UVB. Immunohistochemical analyses of skin papillomas using anti-PCNA, -p53, -involucrin, and -keratin antibody, revealed no difference between the chemical- and UVB-induced papillomas (data not shown). Thus the DMBA–TPA-induced mouse skin tumor model was useful to examine the effect of PDT.

In conclusion, EC036-PDT using 670 nm diode laser showed potent anti-tumor effects in DMBA and TPA-induced mouse skin tumor model. EC036-PDT might be more useful than ATX-S10(Na)-PDT for the treatment of skin tumors.

References

[1] Kurwa HA, Barlow RJ. The role of photodynamic therapy in dermatology. Clin Exp Dermatol 1999;24:143–8.
[2] Morton CA, Brown SB, Collins S, Ibbotson S, Jenkinson H, Kurwa H, et al. Guideline for topical photodynamic therapy: report of a workshop of the British Photodermatology Group. Br J Dermatol 2002;143:552–67.
[3] Ormrod D, Javis B. Topical aminolevulinic acid HCl photodynamic therapy. Am J Clin Dermatol 2000;1:133–9.
[4] Tajiri H, Yokoyama K, Boku N, Ohtsu A, Fujii T, Yoshida S, et al. Fluorescent diagnosis of experimental gastric cancer using a tumor-localizing photosensitizer. Cancer Lett 1997;111:215–20.
[5] Nakajima S, Sakata I, Hirano T, Takemura T. Therapeutic effect of interstitial photodynamic therapy using ATX-S10(Na) and a diode laser on radio-resistant SCC II tumors of C3H/He mice. Anticancer Drugs 1998;9:539–43.
[6] Takahashi H, Itoh Y, Nakajima S, Sakata I, Iizuka H. A novel ATX-S10(Na) photodynamic therapy for human skin tumors and benign hyperproliferative skin. Photodermatol Photoimmunol Photomed 2004;20:257–65.
[7] Takahashi H, Nakajima S, Sakata I, Ishida-Yamamoto A, Iizuka H. Photodynamic therapy using a novel photosensitizer, ATX-S10(Na): comparative effect with 5-aminolevulinic acid on squamous cell carcinoma cell line, SCC15, ultraviolet B-induced skin tumors, and phorbol ester-induced hyperproliferative skin. Arch Dermatol Res 2005;296:496–502.
[8] Wolf P, Rieger E, Kerl H. Topical photodynamic therapy with endogenous porphyrin after application of 5-aminolevulinic acid: an alternative treatment modality for solar keratosis, superficial squamous cell carcinoma, and basal cell carcinoma? J Am Acad Dermatol 1993;28:17–21.
[9] Fijian S, Honigsmann H, Ortel B. Photodynamic therapy of epithelial skin tumors using delta-aminolevulinic acid and desferrioxamine. Br J Dermatol 1995;133:282–8.
[10] Calzavara-Pinton PG. Repetitive photodynamic therapy with topical D-amino-levulinic acid as an appropriate approach to the routine treatment of superficial non-melanoma skin tumors. J Photochem Photobiol B 1995;29:53–7.

Hidetoshi Takahashi[a,*], Susumu Nakajima[b], Ryuji Asano[c], Yoshinori Nakae[c], Isao Sakata[c], Hajime Iizuka[a]

[a]Department of Dermatology, Asahikawa Medical College, 2-1-1-1 Midorigaokahigashi, Asahikawa 078-8510, Japan
[b]Moriyama Memorial Hospital, Japan
[c]Photochemical Co. Ltd., 5319-1 Haga, Okayama 701-1221, Japan

*Corresponding author. Tel.: +81 166682523
E-mail address: ht@asahikawa-med.ac.jp
(H. Takahashi)

16 December 2008

Letter to the Editor

Higher density of label-retaining cells in gingival epithelium

Epithelial sheets made of cultured oral mucosal epithelial cells have been used to treat various epithelial defects [1]. These epithelial sheets are derived from oral epithelial stem cells exhibiting high proliferation potential. In the skin, research into the keratinocyte stem cell niche has advanced remarkably. However, the oral mucosal stem cell niche is less well understood. Thus, we investigated the density of label-retaining cells (LRC) in different areas of oral mucosa to elucidate the localization of oral mucosal stem cells.

Several markers for stem cells have been reported [2]. However, no definite immunohistochemical oral mucosal stem cell marker has yet been established. Stem cells are very slow cycling cells and retain 5-bromo-2'-deoxyuridine (BrdU) label in the nucleus over several weeks [3–5]. Thus, stem cells can be detected as label-retaining cells by BrdU pulse-chase experiments.

We performed BrdU pulse-chase experiments in C57BL/6J mice as previously described [5,6]. For BrdU incorporation studies, the mice ($n = 40$) at 4 weeks of age were given sterile phosphate-buffered saline (PBS) containing BrdU (Roche applied science, Mannheim, Germany) at 0.8 mg/ml. The mice were maintained with PBS drinking fluids containing BrdU for 10 days. Subse-

quently, the mice were transferred to normal drinking water and five mice were sacrificed every 5 days from 20 days after withdrawal of BrdU-labeling to examine the disappearance of BrdU-labeled cells. Frozen sections were made from the oral mucosal tissue of each mouse and BrdU-positive cells were detected by immunofluorescent stain using anti-BrdU antibody (BrdU Labeling and Detection Kit 1, Roche applied science, Mannheim, Germany).

We studied the slow cycling cells using a label retaining technique in six oral areas; dorsum linguae, inferior surface of the tongue, buccal mucosa, palate, gingiva and alveolar mucosa (Fig. 1). In the areas, the rates of LRC expressed as a percentage of the basal layer oral keratinocytes were examined. On day 1, the next day after the last day of BrdU treatment, the rates of LRCs compared to all basal cells were almost 100% in all areas. The rates of all the areas decreased rapidly and became 10% or less by day 20. In previous studies by Bickenbach and Chism [4] and by Ando et al. [5], LRCs were investigated on day 30 and on day 45, respectively. In addition, after 35 days chasse period, the rate of LRCs of each site seems to reach a plateau (Fig. 2). Thus, we considered that only BrdU-positive cells present after day 35 were LRCs in the present experiments. We performed statistical analysis of LRC rates at day 35 and at day 45.

The rates of BrdU-labeled cells in keratinized regions like the gingiva and the palate were higher than that of other non-keratinized areas from day 20 to day 30 (Fig. 2). These results might reflect a difference in the turnover rates because non-keratinized epithelium has a greater turnover rate than keratinized epithelium [7].

Our study showed that, in thick epithelia forming epithelial ridges, LRCs were seen at the bottom of epithelial ridges (Fig. 1). In contrast, in thin epithelia without epithelial ridges, LRCs were located randomly throughout the basal layer cells.
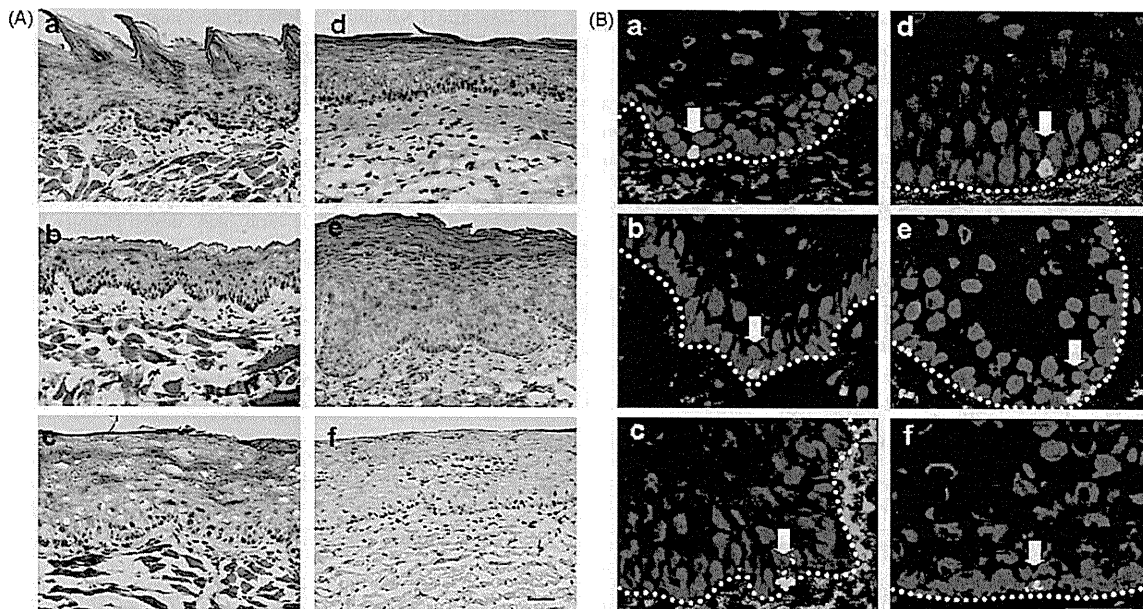
Fig. 1. Localization of label-retaining cells (LRC) in specific regions of oral mucosa. (A) Morphology of each part of oral mucosa (hematoxylin and eosin stain). The epithelium with epithelial ridges was seen in dorsum linguae (a), inferior surface of tongue (b), buccal mucosa (c), and gingiva (e), although the epithelium in palate (d) and alveolar mucosa (f) showed only small epithelial ridges. (B) Immunofluorescent localization of LRCs (arrows) in each part of the oral mucosa at day 50. LRCs were restricted to the basal layer in all the regions. In epithelia with epithelial ridges (panel B-a–c, e), LRCs were seen at the bottom of epithelial ridges. (a) Dorsum linguae, (b) inferior surface of tongue, (c) buccal mucosa, (d) palate, (e) gingival, (f) alveolar mucosa. BrdU labeling, fluorescein isothiocyanate (green); nuclear stain, propidium idodide (red). White dotted line, the basement membrane zone. Bars, 50 μm.
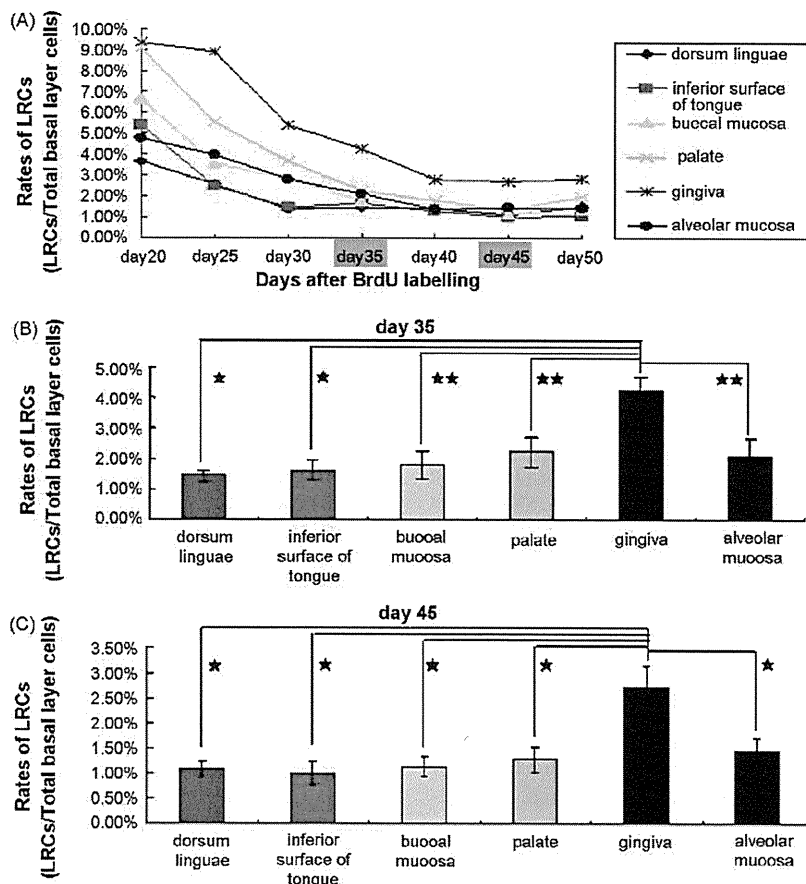
Fig. 2. LRC counts in the oral mucosal epithelium. (A) The rates of BrdU-positive cells to total basal layer keratinocyte numbers from day 20 to day 50. BrdU-positive cells at day 35 and later were considered to be LRCs, the rates of LRCs in the gingiva were significantly higher than those of the other parts in the oral mucosa. (B) Rates of LRCs in each part of oral mucosa at day 35. The rate of LRCs in the gingiva were significantly higher than that in the other parts of the oral mucosa ($^*P < 0.05$; $^{**}P < 0.01$). (C) Rates of LRCs in each part of oral mucosa at day 45. As well as day 35, the rate of LRCs in the gingiva were significantly higher ($^*P < 0.05$).

Interestingly, after day 35, the rates of LRCs in the gingiva were remarkably higher than in the other oral mucosa areas (Fig. 2). At day 35, the rates of LRCs to basal cells were as follows; dorsum linguae, 1.45%; inferior surface of tongue, 1.63%; buccal mucosa, 1.80%; palate, 2.23%; gingival, 4.28%; alveolar mucosa, 2.09%. The existence of LRCs provides no direct indication that such cells are functioning as a subpopulation of stem cells [3]. However, it was thought that the high rates of LRCs in the gingival might reflect a high density of slow-cycling cells, suggesting that there might be a relatively larger number of stem cells in gingival epithelium.

The oral mucosa epithelium comprises stratified squamous epithelium, which may be keratinized or non-keratinized, depending on the region of the oral cavity [1]. The palatal and gingival mucosae are categorized as a masticatory mucosa and their epithelial layer is thick and keratinized or para-keratinized to withstand biting and masticatory stress. The inferior surface of the tongue, buccal mucosa and alveolar mucosa are categorized as a lining mucosa. Their epithelial layers are mostly non-keratinized. The dorsum linguae are classified as a specialized mucosa with several kinds of lingual papillas and their epithelial layers including the filiform papillae show keratinization. The structure of each oral mucosal region in mice was similar to that of the corresponding part in humans.

Examination of hamster palatal papillae showed that the majority of label-retaining cells were located in the deepest part of the epithelial ridges [8]. In this report, any part of oral mucosa epithelium with prominent epithelial ridges had LRCs specifically at the bottom of the ridges without forming a cluster.

The keratinized oral gingival epithelium provides effective protection for underlying tissue against mechanical trauma and dental bacterial invasion. The non-keratinized junctional epithelia with high turnover rates have a basic attachment function to the tooth and form an effective barrier to bacterial penetration [9]. To maintain intact gingiva at the forefront of defense mechanism, a higher density of stem cells might be necessary in the gingival epithelium.

During oral reconstructive surgery, selection of a donor site for mucosal epithelial cell collection is an important agenda. To obtain an epithelial sheet, 15 cm² in size, a 4–8 mm² mucosal resection is needed [10]. The buccal mucosa has been thought to be an appropriate donor site. Probably collection of the gingival epithelium in surgical procedures such as wisdom tooth extraction and periodontal surgery is a relatively easy way to collect sufficient oral mucosal stem cells. The present results suggest that the gingival epithelium might be a preferable source for collection of oral mucosal epithelial cells for oral mucosal reconstruction treatment.

Acknowledgments

References

[1] Moharamzadeh K, Brook IM, Van Noort R, Scutt AM, Thornhill MH. Tissue-engineered oral mucosa: a review of the scientific literature. J Dent Res 2007;86:115–24.

[2] Grisanzio C, Signoretti S. p63 in prostate biology and pathology. J Cell Biochem 2008;103:1354–68.

[3] Bickenbach JR. Identification and behavior of label-retaining cells in oral mucosa and skin. J Dent Res 1981;60:1611–20.

[4] Bickenbach JR, Chism E. Selection and extended growth of murine epidermal stem cells in culture. Exp Cell Res 1998;244:184–95.

[5] Ando S, Abe R, Sasaki M, Murata J, Inokuma D, Shimizu H. Bone marrow-derived cells are not the origin of the cancer stem cells in ultraviolet-induced skin cancer. Am J Pathol 2009;174:595–601.

[6] Tough DF, Sprent J. Turnover of naive- and memory-phenotype T cells. J Exp Med 1994;179:127–35.

[7] Thomson PJ, Potten CS, Appleton DR. Mapping dynamic epithelial cell proliferative activity within the oral cavity of man: a new insight into carcinogenesis? Br J Oral Maxillofac Surg 1999;37:377–83.

[8] Bickenbach JR, Mackenzie IC. Identification and localization of label-retaining cells in hamster epithelia. J Invest Dermatol 1984;82:618–22.

[9] Schroeder HE, Listgarten MA. The gingival tissues: the architecture of periodontal protection. Periodontology 2000 1997;13:91–120.

[10] Sauerbier S, Gutwald R, Wiedmann-Al-Ahmad M, Lauer G, Schmelzeisen R. Clinical application of tissue-engineered transplants. Part I. Mucosa. Clin Oral Implants Res 2006;17:625–32.

Takuya Asaka[a,b],
Masashi Akiyama[a,*],
Yoshimasa Kitagawa[b],
Hiroshi Shimizu[a]

[a]Department of Dermatology,
Hokkaido University Graduate School of Medicine,
North 15 West 7, Kita-ku, Sapporo 060-8638, Japan
[b]Oral Diagnosis and Oral Medicine,
Department of Oral Pathobiological Science,
Hokkaido University Graduate School of Dental Medicine, Japan

*Corresponding author. Tel.: +81 11 716 1161x5962;
fax: +81 11 706 7820
E-mail address: akiyama@med.hokudai.ac.jp
(M. Akiyama)

13 November 2008

Letter to the editor

Inhibition of protein kinase CK2 induces E2F1 nuclear export, formation of p21/E2F1 complexes and suppression of DNA synthesis in normal human epidermal keratinocytes

Protein kinase CK2 (formerly termed "casein kinase II") is an extremely conserved Ser/Thr kinase, which is ubiquitously distributed in eukaryotic cells. CK2 is quite unique enzyme, strongly distinguished from others protein kinases by particularly two properties—high constitutive activity and lack of an acute mechanism/s of regulation. The extreme pleiotropy (with list of over 300 substrates) is another of its characteristic [1]. Despite of the gaps in understanding of precise molecular mechanisms the

importance of CK2 in the context of signal transduction, gene expression and respectively in the cell regulation, including the maintenance of cell cycle is incontestable.

To gain information about CK2 role in the signal transduction control of keratinocyte cell cycle, we investigated its involvement in the regulation of a crucial transcriptional factors c-Myc and E2F1 by taking advantage of CK2 very selective cell-permeant inhibitor 4, 5, 6, 7-tetrabromobenzotriazole (TBB) (Calbiochem, Darmstadt, Germany).

E2F1 is one of the eight different (E2F1 through -8) members of E2F family of transcription factors, which is essential for cell cycle progression, since it initiates transcription of the genes required for

Epithelial and Mesenchymal Cell Biology

Type XVII Collagen is a Key Player in Tooth Enamel Formation

Takuya Asaka,*[†] Masashi Akiyama,*
Takanori Domon,[‡] Wataru Nishie,* Ken Natsuga,*
Yasuyuki Fujita,* Riichiro Abe,*
Yoshimasa Kitagawa,[†] and Hiroshi Shimizu*

From the Department of Dermatology, Hokkaido University
Graduate School of Medicine, Sapporo; Oral Diagnosis and Oral
Medicine,[†] the Department of Oral Pathobiological Science, and
the Division of Oral Functional Science,[‡] the Department of Oral
Functional Anatomy, Hokkaido University Graduate School of
Dental Medicine, Sapporo, Japan*

Inherited tooth enamel hypoplasia occurs due to mu-
tations in genes that encode major enamel compo-
nents. Enamel hypoplasia also has been reported in
junctional epidermolysis bullosa, caused by muta-
tions in the genes that encode type XVII collagen
(COL17), a component of the epithelial-mesenchymal
junction. To elucidate the pathological mechanisms
of the enamel hypoplasia that arise from the defi-
ciency of epithelial-mesenchymal junction mole-
cules, such as COL17, we investigated tooth formation
in our recently established $Col17^{-/-}$ and $Col17$ res-
cued mice. Compared with wild-type mice, the inci-
sors of the $Col17^{-/-}$ mice exhibited reduced yellow
pigmentation, diminished iron deposition, delayed
calcification, and markedly irregular enamel prisms,
indicating the presence of enamel hypoplasia. The
molars of the $Col17^{-/-}$ mice demonstrated advanced
occlusal wear. These abnormalities were corrected in
the $Col17$ rescued humanized mice. Thus, the
$Col17^{-/-}$ mice clearly reproduced the enamel hyp-
oplasia in human patients with junctional epidermol-
ysis bullosa. We were able to investigate tooth forma-
tion in the $Col17^{-/-}$ mice because the $Col17^{-/-}$
genotype is not lethal. $Col17^{-/-}$ mouse incisors had
poorly differentiated ameloblasts that lacked enamel
protein-secreting Tomes' processes and reduced mRNA
expression of amelogenin, ameloblastin, and of other
enamel genes. These findings indicated that COL17 reg-
ulates ameloblast differentiation and is essential for
normal formation of Tomes' processes. In conclusion,
COL17 deficiency disrupts the epithelial-mesenchymal
interactions, leading to both defective ameloblast differ-
entiation and enamel malformation. *(Am J Pathol 2009,
174:91–100; DOI: 10.2353/ajpath.2009.080573)*

Mesenchymal-epithelial interactions are thought to play
essential roles in development of epithelial organs includ-
ing the epidermis, hair follicles, and teeth. A variety of
soluble factors, cell surface markers, and signal mole-
cules have been reported to be involved in mesenchy-
mal-epithelial interactions.[1,2] The hemidesmosome is a
subcellular junctional adhesion structure overlying the
basement membrane between the mesenchyme and ep-
ithelial cells that binds the epithelial cells to the underly-
ing mesenchymal tissue.[3] Type XVII collagen (COL17)
previously called "bullous pemphigoid antigen 2" or
"BP180," is a transmembrane glycoprotein expressed in
stratified and complex epithelia, such as the skin, the
mucous membrane, and the eye, where it plays a crucial
role in hemidesmosome stability and epithelial-mesen-
chymal attachment.[4]

Non-Herlitz junctional epidermolysis bullosa (nH-JEB)
caused by COL17 deficiency shows the abnormal tooth
formation of amelogenesis imperfecta.[5–7] We therefore
hypothesized that COL17 in hemidesmosomes also plays
an important role in mesenchymal-epithelial interactions
in tooth formation.

Enamel formation is easily disrupted and enamel de-
fects may reflect more than just genetic abnormalities.
Enamel defects can also be attributed to environmental
factors that cause chronological hypoplasia of the
enamel during the enamel formation period.[7] It is impor-
tant to study the pathomechanisms of enamel malforma-
tion in mice with defects in hemidesmosome components.
There are several model mice with epithelial mesenchymal
junction (EMJ) component deficiencies.[3,8] Among them,
only laminin332-deficient mice are expected to have tooth
malformation. However, the laminin332 knockout mice are

91

lethal in their early development and tooth abnormality in adult mice has not been examined sufficiently.[8]

The *Col17* knockout (*Col17*$^{-/-}$) mice that we established recently are not lethal at birth; thus, we can use them to investigate the pathomechanisms of enamel defects that arise from hemidesmosome component deficiency.

To clarify the roles of COL17 in tooth formation, we studied the detailed process of tooth formation in *Col17* knockout (*Col17*$^{-/-}$) mice, which we recently established.[9] We show that COL17 has a critical role in tooth formation, especially in the differentiation of ameloblasts and enamelization, suggesting the importance of junction structure in mesenchymal-epithelial interaction during tooth formation.

Materials and Methods

Generation of *Col17*$^{-/-}$ Mice and Rescued COL17-Humanized Mice

The procedure for generating COL17$^{-/-}$ mice has been described.[9] Briefly, we cloned a 14.7-kb mouse genomic DNA COL17 fragment from the mouse 129Sv/Ev genomic library (Stratagene, La Jolla, CA). We subcloned a 11.5-kb *Nhe*I to *Not*I fragment to make the targeting vector. We inserted the PGK/Neo cassette between 6-bp upstream of the ATG start codon in exon 2 and 1.2-kb downstream in intron 2. We transfected the targeting vector by electroporation into 129 Sv/Ev embryonic stem cells, then microinjected the correctly targeted embryonic stem cell line into blastocysts obtained from C57BL/6J mice (Jackson Laboratory, Bar Harbor, Maine) to generate chimeric mice, which we then mated with C57BL/6J females. We crossed F1 heterozygotes with C57BL/6J for more than four generations and then intercrossed them to generate *Col17*$^{-/-}$ mice. The procedures for screening *Col17*$^{-/-}$ mice by PCR, reverse transcription (RT)-PCR, Northern and Western blotting, histology, electron microscopy, and immunofluorescence are described elsewhere.[9]

The phenotypic features of the *Col17* knockout (*Col17*$^{-/-}$) mice closely resembled those seen in nH-JEB (OMIM: 226650) caused by null mutations in the *COL17A1* gene, as previously described.[9] The *Col17*$^{-/-}$ mice had skin blisters and erosions from mild trauma. *Col17*$^{-/-}$ mice skin showed subepidermal blistering associated with a lack of COL17 and poorly formed hemidesmosomes.

Procedures for generating COL17-rescued mice have been described elsewhere.[9] Briefly, we crossed transgenic mice (C57BL/6 background) expressing the squamous epithelium-specific K14 promoter and a human *COL17* cDNA (*Col17*$^{m+/+}$ *COL17*$^{h+}$) with heterozygous *Col17*$^{m+/-}$ mice. Mice that carried both the heterozygous null mutation of *Col17* and the transgene of human *Col17* (*Col17*$^{m+/-}$ *COL17*$^{h+}$) were bred to produce rescued *Col17*$^{m-/-}$, *COL17*$^{h+}$ COL17-humanized mice.

The rescued mice showed almost none of the abnormal manifestations seen in the *Col17*$^{-/-}$ mice.[9]

Structural Analysis of Mouse Dentition

Tissue samples of mice were incubated in hot (approximately 90°C) distilled water for several minutes, and soaked in 10% Tasinase (Kyowa-hakkou, Tokyo, Japan) at 37°C for 6 hours. Incisors and first molars were taken from maxillomandibular tissue by removal of soft tissue. The teeth were carefully cleaned and were observed macroscopically. After air-drying overnight, the teeth were sputter-coated with carbon CC-40F (Meiwa-shouji, Osaka, Japan), and were observed with a Hitachi S-4000 scanning electron microscope (Hitachi Electronics, Tokyo, Japan) operated at 15 kV. For the observation of enamel rod inclination, sagittal sections of maxillary incisors were etched by a grinder for 30 seconds in 0.1N hydrochloric acid and were observed similarly.

Chemical and Mineralization Analyses

Qualitative and distributive elemental analysis was performed in sagittal sections of maxillary incisors prepared with a grinder and in the labial side of maxillary incisors with a Hitachi S-2380 scanning electron microscope (Hitachi, Tokyo, Japan) operated at 15kV and energy dispersive X-ray spectrometry (EDX).

To demonstrate the patterns of mineralization, radio transparencies of the contact microradiographs were examined as previously described.[10] Maxillary incisors were dehydrated by passage through a series of ascending concentrations of ethanol solutions and embedded in polyester resin (Rigolic, Ouken Co., Tokyo, Japan). Longitudinal labio-lingual ground sections of 100-μm thickness were prepared with a rotary diamond saw (Speadrap ML521; Maruto, Tokyo, Japan) and emery papers. Microradiographs of the ground sections were recorded on Kodak SO-181 high-resolution film (Eastman Kodak, Rochester, NY) using a cabinet X-ray apparatus (CSM-2; Softex, Tokyo, Japan) at 15 kV, 4 mA for 20 minutes. The films were developed, fixed, and observed under a light microscope.

Preparation of Tissue Sections and Immunohistochemistry

Under anesthesia with ether inhalation, intracardiac perfusions for 2-week-old mice were performed with a fixative solution containing 4% paraformaldehyde in PBS, pH 7.4. Postfixation was ensured by immersion of dissected maxilla and mandible in the fixative solution overnight at 4°C.

The maxillae and mandibles with incisors were processed for histological analysis by decalcification at 4°C for up to 2 weeks in a pH 7.4 PBS solution containing 10% EDTA. After extensive washing in PBS, the samples were dehydrated in increasing concentrations of ethanol and lemosol (Wako, Osaka, Japan), and were finally embedded in paraffin. Serial longitudinal and frontal sections of the incisors of the paraffin-embedded specimens (5 μm) were processed for H&E staining.
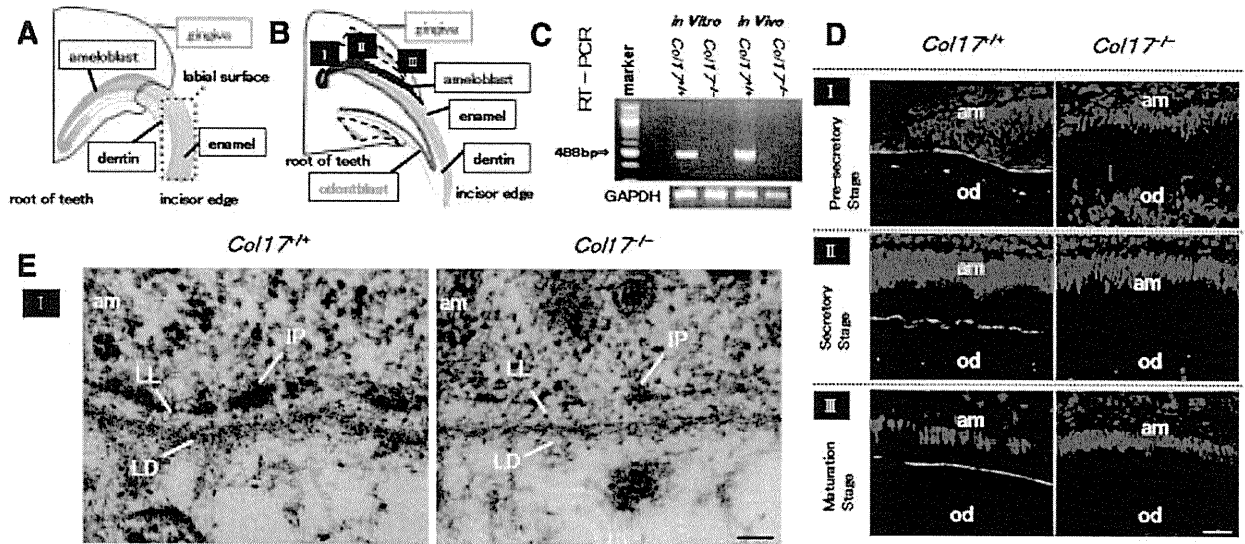
Figure 1. COL17 expression in the tooth of $Col17^{+/+}$ mice and COL17 absence in the tooth of $Col17^{-/-}$ mice. **A, B:** Mouse incisors are continuously elongating teeth. In the root of these incisors, ameloblasts (blue) and odontoblasts (green) secrete enamel matrix and dentin, respectively, during the secretory stage (II). I: the pre-secretory stage; II: the secretory stage; III: the maturation stage. **C:** A RT-PCR assay revealed that $Col17$ mRNA (488 bp band) was expressed in cultured ameloblasts from $Col17^{+/+}$ mice (**left lane**) and $Col17^{+/+}$ mouse teeth (**second right**). $Col17$ mRNA was not expressed in cultured ameloblasts from $Col17^{-/-}$ mice (**second left lane**) or $Col17^{-/-}$ mouse teeth (**right hand lane**). **D:** Immunofluorescence staining for COL17 (green) revealed that COL17 was expressed in the EMJ between ameloblasts and odontoblasts at the pre-secretory stage of a $Col17^{+/+}$ mouse (**upper, left**), between ameloblasts and enamel matrix in the secretory stage (**middle, left**) and in the maturation stage (**lower, left**) of a $Col17^{+/+}$ mouse. At the secretory stage, COL17 expression was weak, intermittent, or absent. In $Col17^{-/-}$ mice, no COL17 staining was observed in the EMJ at any stage (**right column**). am: ameloblast; od: odontblast. Scale bar = 20 μm. **E:** Ultrastructural features of the basement membrane zone at the pre-secretory stage. Normal hemidesmosomes were seen in the $Col17^{+/+}$ mouse (**left**), but hypoplastic, malformed hemidesmosomes were observed in the $Col17^{-/-}$ mice (**right**). am: ameloblast; LL: lamina lucida; IP: inner attachment plaques; LD :lamina densa. Scale bar = 60 nm.

For immunohistochemistry, neonatal mice (day-1) were sacrificed and the tissue samples were embedded in optimal cutting temperature compound (Sakura Finetechnical Co., Tokyo, Japan) for frozen sectioning. Frozen tissue sections were cut at a thickness of 6 μm sagittally until incisors were exposed, or coronally until molars were exposed. Sections were fixed with acetone for 10 minutes at −20°C, and washed in PBS, incubated with a primary antibody, anti-mouse COL17 monoclonal antibody (NC-16A, final dilution, 1:2500), at 37°C for 30 minutes. Then, the sections were incubated with a secondary antibody, fluorescein isothiocyanate (FITC)-conjugated goat anti-rat IgG (H+L; Jackson ImmunoResearch Laboratories, Suffolk, UK; final dilution, 1:50), at 37°C for 30 minutes, and incubated with 10 μg/ml of propidium iodide at 37°C for 10 minutes for nuclear counterstaining. Sections were observed under an Olympus Fluoview confocal laser-scanning microscope (Olympus, Tokyo, Japan).

Ultrastructural Analysis during Tooth Formation

As above, from the maxillomandibular tissue fixed with modified Karnovsky's fixative (at a final concentration of 2% paraformaldehyde and 2.5% glutaraldehyde in 0.05 mol/L cacodylate buffer solution, pH 7.4), 2-week-old mice incisors were obtained and decalcified in 10% EDTA pH 7.4, at 4°C for 2 weeks. After decalcification, samples were postfixed in 1% osmium tetroxide at 4°C for 2 hours and stained en bloc with 1% uranyl acetate at 4°C for 20 minutes. The samples were dehydrated through a graded series of ethanol and embedded in Epon 812

(TAAB Laboratories, Berkshire, UK). Ultrathin sections were cut in the sagittal direction to include both the separated enamel organ and the dental papilla. Sections were stained with uranyl acetate and lead citrate, and observed under a Hitachi H-7000 transmission electron microscope (Hitachi, Tokyo, Japan).
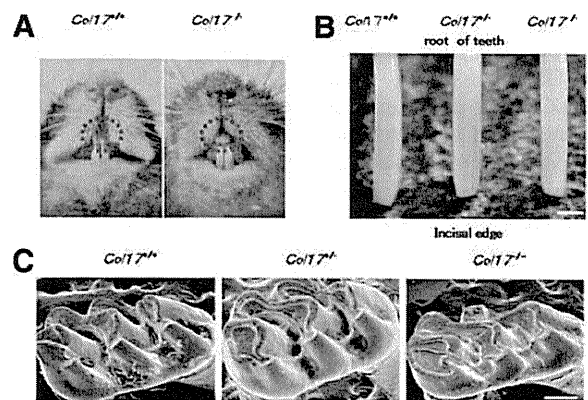
Figure 2. Dental phenotype of $Col17^{-/-}$ mice. **A:** At 4 weeks of age, a $Col17^{-/-}$ mouse (**right**) had whitish incisors. **B:** Incisors from $Col17^{+/+}$ and $Col17^{+/-}$ mice showed yellowish color, although an incisor from a $Col17^{-/-}$ mouse seemed whitish (**right**). Scale bar = 500 μm. **C:** In the molars, tooth wear was more advanced for the $Col17^{-/-}$ mice (**right**) than for the $Col17^{+/+}$ (**left**) and $Col17^{+/-}$ (**center**) mice. Scale bar = 250 μm.
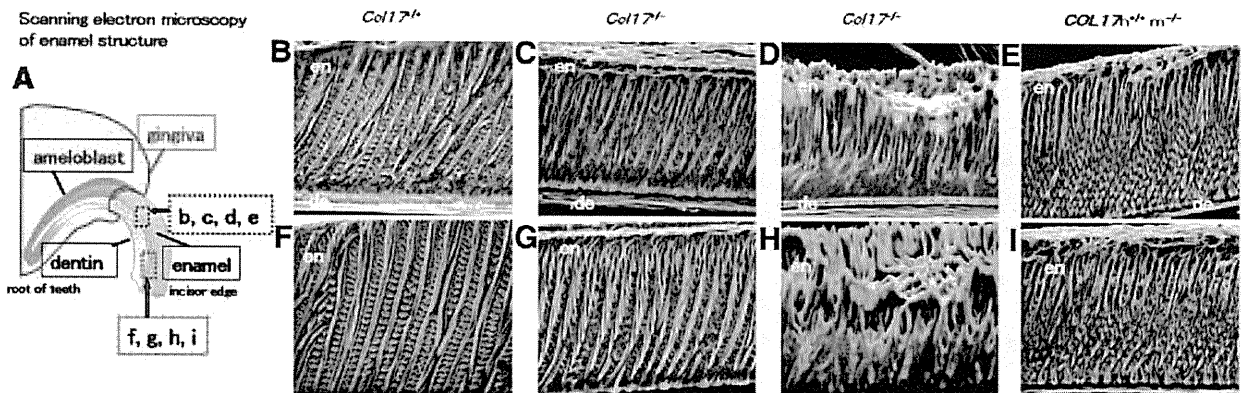
Figure 3. Scanning electron microscopy of the sagittal section of maxillary incisors. **A:** A model of an upper incisor. The enamel layer indicated by an **upper blue rectangle** and by a **lower red rectangle** is enlarged in **B, C, D** and **E**, and in **F, G, H** and **I**, respectively. In the $Col17^{-/-}$ mouse, irregular inclinations of enamel rods without a normal network arrangement are observed (**D, H**), in contrast to the regular network of enamel rods observed in the $Col17^{+/+}$ incisor (**B, F**) and in the $Col17^{+/-}$ incisor (**C, G**). The normal, regular network of enamel rods has been restored in the COL17 humanized mouse (**E, I**). en: enamel; de: dentin. Scale bar = 20 μm.

Terminal Deoxynucleotidyl Transferase-Mediated dUTP Nick-End Labeling Staining

For the detection of apoptotic cells in the ameloblast layer by terminal deoxynucleotidyl transferase-mediated dUTP nick-end labeling (TUNEL) assay, paraffin sections were processed with *in situ* apoptosis detection kits (Apoptag; Chemicon International, Temecula, CA).[11] The number of apoptotic ameloblasts at each stage was calculated based on the criterion that an apoptotic body of more than 2 μm in diameter could be defined as a count; these numbers were compared between $Col17^{+/+}$ and $Col17^{-/-}$.

Cell Cultures and Immunolabeling

For dental epithelial cell cultures, maxillary and mandibular incisors from 2-week-old mice were dissected, and the distal part of the incisors was removed. Tooth samples were treated with 0.25% trypsin for 10 minutes and pipetted up and down intensely. The dental epithelial cells, dental mesenchymal cells, and various other cells were isolated from incisors. To separate dental epithelial cells from the other cells, cells were cultured in epidermal keratinocyte medium containing a small amount of bovine pituitary extract (CNT-57; CELLnTEC Advanced Cell Systems, Bern, Switzerland) for 7 days. After obtaining a sufficient number of dental progenitor epithelial cells, we changed the culture medium to epidermal keratinocyte medium containing 0.07 mmol/L calcium (CNT-02; CELLnTEC Advanced Cell Systems, Bern, Switzerland) to induce differentiation, and cultured it for 10 days.

For fluorescence staining, the cells were fixed with 70% ethanol for 10 minutes and washed with PBS. The cells were incubated with a primary antibody anti-mouse amelogenin polyclonal antibody (Hokudo, Sapporo, Japan), final dilution of 1:100 or with anti-mouse ameloblastin polyclonal antibody (Santa Cruz Biotechnology, Santa Cruz, CA), final dilution, 1:50, at 37°C for 30 minutes. Then, the cells were incubated with the secondary anti-body FITC-conjugated goat anti-rabbit IgG (H+L; Jackson ImmunoResearch Laboratory, West Grove, PA), final dilution, 1:50, or with FITC-conjugated donkey anti-goat IgG (H+L; Jackson ImmunoResearch Laboratory, West Grove, PA), final dilution, 1:50, at 37°C for 30 minutes and incubated with 10 μg/ml of propidium iodide at 37°C for 10 minutes to visualize the nucleus. The cells were observed under an Olympus FluoView confocal laser-scanning microscope (Olympus, Tokyo, Japan).

RT-PCR Analysis

To study *Col17* mRNA expression in dental epithelial cells and ameloblasts, total RNA from incisors or cultured dental epithelial cells was extracted using TRIZOL reagent (Invitrogen, Carlsbad, CA), according to the manufacturer's instructions. Extracted RNA was used for cDNA synthesis in SuperScript III reverse transcriptase (Invitrogen, Carlsbad, CA) according to the manufacturer's instructions. The following primers specific for mouse *Col17* sequence (NM: 007732) were used for RT-PCR: 5'-AGAAGAAAA GCATC-CGAGGG-3' (RT-F); and 5'-TGGTTGAAGAAGAGGC-GAGT-3' (RT-B). As a control, we used the primers for mouse glyceraldehyde-3-phosphate dehydrogenase (GAPDH; NM: 001001303): 5'-TTAGCCCCCCTGGC-CAAGG-3' (mGAPDH-F) and 5'-CTTACTCCTTGGAG-GCCATG-3' (mGAPDH-B), which amplified a 541-bp fragment.

Real-Time RT-PCR Analysis

To quantitatively analyze mRNA expression levels of tooth-formation-associated proteins, amelogenin, ameloblastin, enamelin, tuftelin, enamelysin, and dentin sialophosphoprotein (DSPP), in teeth from the $Col17^{+/+}$ and $Col17^{-/-}$ mice, cDNA samples were analyzed using the ABI prism 7000 sequence detection system (Applied Biosystems, Foster City, CA). Primers and probes specific for amelogenin, ameloblastin, enamelin, tuftelin, enamelysin, DSPP, and control housekeeping genes, GAPDH and β-ac-
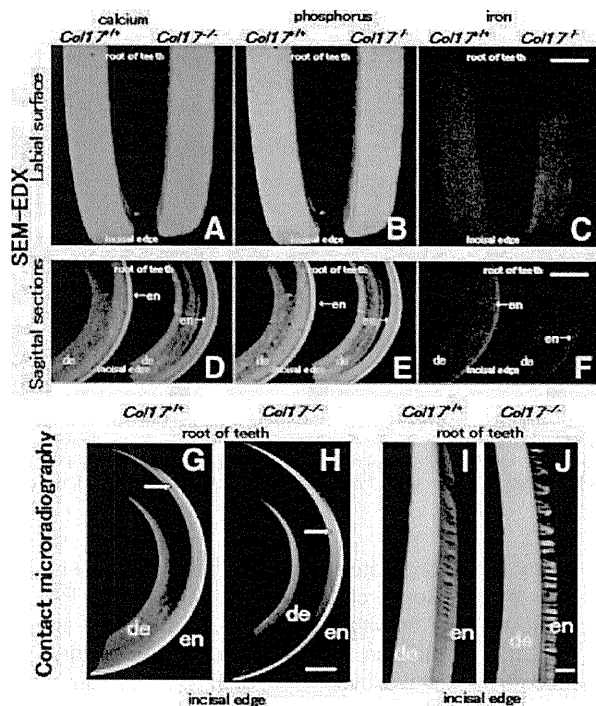
Figure 4. Difference in enamel formation between $Col17^{+/+}$ and $Col17^{-/-}$ mice incisors. The labial surface (see Figure 1A) is featured in **A**, **B**, and **C**. A sagittal section is shown in **D**, **E**, and **F**. **A**, **B**: The labial surface of the maxillary incisors in both $Col17^{+/+}$ (**left**) and $Col17^{-/-}$ (**right**) mice was scanned for calcium (green) and phosphorus (yellow) with EDX spectrometry. No obvious difference was observed in elemental distribution mapping. **C**: The same surfaces scanned in EDX for iron (red). In $Col17^{-/-}$ mice (**right**), the distribution of iron was irregular, compared with that of a $Col17^{+/+}$ mice (**left**). Scale bar: (**A, B, C**) = 500 µm. **D, E, F**: The sagittal sections of the maxillary incisors of both $Col17^{+/+}$ (**left**) and $Col17^{-/-}$ (**right**) mice scanned in EDX for calcium (green), phosphorus (yellow), and iron (red). No obvious difference is observed in the distribution of calcium or phosphorus between the $Col17^{+/+}$ (**left**) and $Col17^{-/-}$ (**right**) mice. In the $Col17^{-/-}$ mice (**right**), the iron concentration in the enamel is lower than that in the $Col17^{+/+}$ mouse (**left; F**). en: enamel; de: dentin. Scale bars in (**D, E, F**) = 1000 µm. **G, H**: Microradiographs of maxillary incisors in $Col17^{+/+}$ (**G**) and $Col17^{-/-}$ (**H**) mice. The position (**arrows**) where sufficient mineralization occurred in the enamel judged from the low radio-opacity signal, moved toward the incisal edge in maxillary incisors of a $Col17^{-/-}$ mouse (**G**), compared with that in incisors of a $Col17^{+/+}$ mouse (**H**). en: enamel; de: dentin. Scale bar: (**G, H**) = 500 µm. **I, J**: Microradiographs showing the mineralization pattern of the developing enamel at the maturation stage from $Col17^{+/+}$ (**I**) and $Col17^{-/-}$ (**J**) mice. As compared with $Col17^{+/+}$ (**I**), the mineralization demonstrated by radio-opacity of the enamel was irregular in both stages in $Col17^{-/-}$ mice (**J**), although there were no differences in the radio-opacity of dentine between $Col17^{+/+}$ (**I**) and $Col17^{-/-}$ (**J**) mice. en: enamel; de: dentin. Scale bar: (**I, J**) = 100 µm.

tin, were obtained from the TaqMan gene expression assay (Applied Biosystems, Foster City, CA; Probe ID; Mm00711644_g1, Mm00477485_m1, Mm00516922_m1, Mm00449139_m1, Mm00600244_m1 and Mm00515666_m1, Mm99999915_gl, Mm00607939_sl).

Differences between the mean CT values of mRNA expressions of tooth-formation-associated proteins and those of GAPDH or ß-actin were calculated as $\Delta CT_{Col17-/- \text{ mice}} = CT_{\text{tooth protein}} - CT_{\text{GAPDH (or other housekeeping genes)}}$ and those of ΔCT for the $Col17^{+/+}$ incisors as $CT_{\text{calibrator}} = CT_{\text{tooth protein}} - CT_{\text{GAPDH (or other housekeeping genes)}}$. Final results for $Col17^{-/-}$ incisor samples/$Col17^{+/+}$ incisor samples (%) were determined by $2^{-(CT\ Col17-/- \ - \ CT\text{calibrator})}$.

Using similar methods, we quantitatively analyzed the tooth-formation-associated protein mRNA expression levels in the dental epithelial cells cultured from the $Col17^{+/+}$ and $Col17^{-/-}$ mice.

Results

COL17 Expression Pattern in the EMJ of Teeth in $Col17^{-/-}$ Mice

We observed the expression of $Col17$ at each of the three stages of enamel formation: pre-secretory, secretory, and maturation (Figure 1, A and B). The 488-bp fragments of mouse $Col17$ mRNA were detected in $Col17^{+/+}$ mouse incisors *in vivo* and in cells cultured from $Col17^{+/+}$ mouse incisors *in vitro*, although mouse $Col17$ mRNA was detected in neither incisors nor cultured cells from $Col17^{-/-}$ mice (Figure 1C).

To clarify COL17 expression during tooth formation, we immunostained tissue sections of maxillary incisors in which we could observe all differentiation stages of tooth formation. COL17 was expressed in the EMJ between ameloblasts and odontoblasts at the pre-secretory stage. Due to elongation of Tomes' processes, the basement membrane became discontinuous and COL17 expression was reduced and in places became intermittent at the secretory stage. COL17 expression reappeared at the maturation stage (Figure 1D).

In the $Col17^{-/-}$ mice, COL17 expression was not observed in the EMJ under the ameloblasts at any stage during tooth development.

The basement membrane on the basal surface of the ameloblasts separates the ameloblasts from mesenchymal tissue/pre-odontoblasts. Hemidesmosomes are observed in the EMJ, and they are composed of prominent inner plaques, outer plaques, and sub-basal dense plates, similar to those in the dermo-epidermal junction in the skin. Anchoring filaments cross the lamina lucida, and anchoring fibrils anchor lamina densa to the mesenchymal tissue in the $Col17^{+/+}$ mice (Figure 1E).

In the $Col17^{-/-}$ mice, there were a reduced number of hypoplastic inner and outer hemidesmosomal attachment plaques with poor keratin filament association and less prominent anchoring filaments, whereas anchoring fibrils and the lamina densa were both normally preserved (Figure 1E).

Dental Phenotype in the $Col17^{-/-}$ Mice

The incisors of wild-type ($Col17^{+/+}$) and heterozygous ($Col17^{+/-}$) mice exhibit yellow pigmentation on the surface. The incisors of the $Col17^{-/-}$ mice had a chalky, whitish appearance (Figure 2, A and B). The $Col17$-rescued mice (mouse $Col17^{-/-}$, human $COL17^{+/+}$) had yellowish incisors, as did the wild-type $Col17^{+/+}$ mice (data not shown). By scanning electron microscopy, the enamel surface of the $Col17^{+/+}$, $Col17^{+/-}$ and $Col17^{-/-}$ mice appeared smooth and unpitted (data not shown). Molar wear was more advanced in the $Col17^{-/-}$ mice than in the $Col17^{+/+}$ and $Col17^{+/-}$ mice. This tooth wear
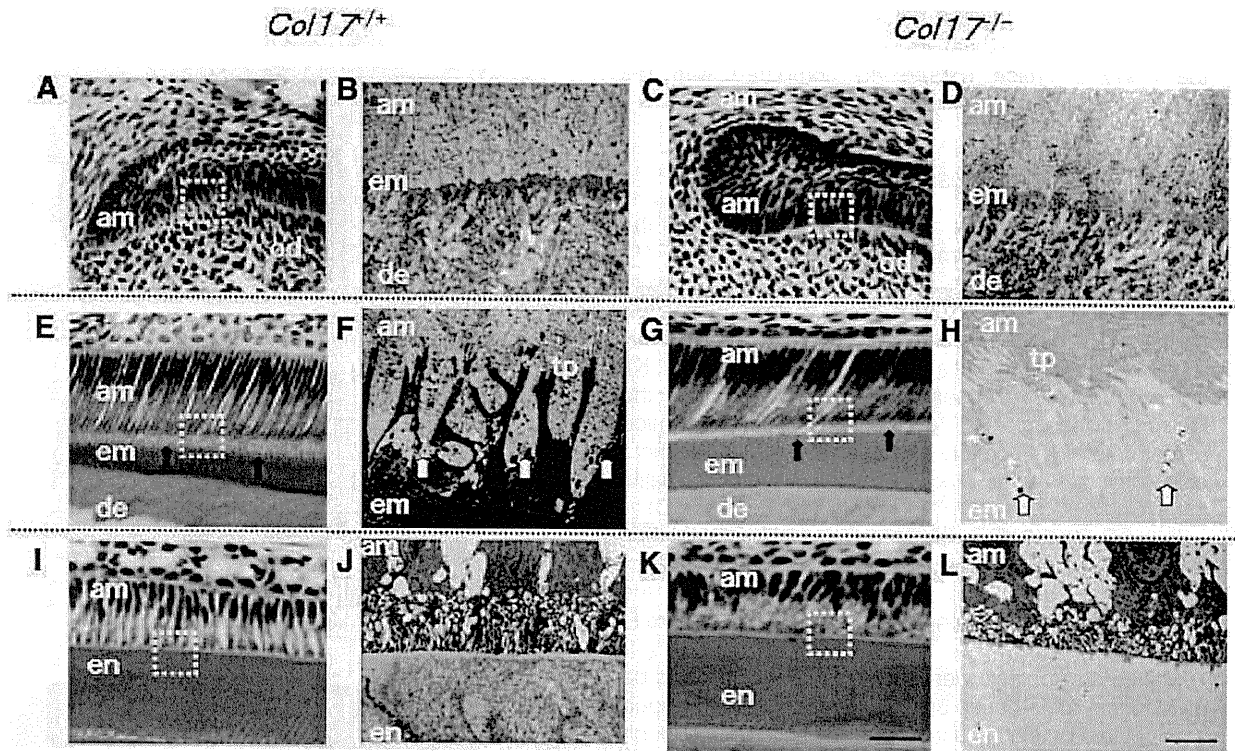
Figure 5. Malformed Tomes' processes and defective amelogenesis in $Col17^{-/-}$ mice **A–D:** At the pre-secretory and early secretory stages, the EMJ separates pre-ameloblasts and pre-odontoblasts. **A, C:** The overall structures of pre-ameloblasts and pre-odontoblasts were similar in the $Col17^{+/+}$ (**A**) and $Col17^{-/-}$ (**C**) mice in the pre-secretory to the early secretory stages at the light microscopic level. **B, D:** Ultrastructurally, from the pre-secretory to the early secretory stages, the basement membrane between ameloblasts and odontoblasts was blurred in the $Col17^{-/-}$ mouse (**D**), compared with more obvious, intact basement membrane structures in a $Col17^{+/+}$ mouse (**B**). **E–H:** At the secretory stage, Tomes' processes are formed and enamel matrix is produced by ameloblasts. **E, G:** In the secretory stage, the processes of ameloblasts were malformed and blurred (**arrows**) in the $Col17^{-/-}$ mouse (**G**), compared with well-organized lattice-like structures of the Tomes' processes (**arrows**) in the $Col17^{+/+}$ mice (**E**). The thickness of the enamel matrix seemed similar both in $Col17^{+/+}$ (**E**) and $Col17^{-/-}$ (**G**) mice. At the secretory stage, Tomes' processes were apparently hypoplastic in the $Col17^{-/-}$ mouse (**H**), compared with normal Tomes' processes in the $Col17^{+/+}$ mouse (**F**). **I–L:** In the maturation stage, disruption of the processes of ameloblasts (am) was more advanced in the $Col17^{-/-}$ mouse (**K**), compared with regular processes in the $Col17^{+/+}$ mice (**I**). At the maturation stage, the electron density of the enamel matrix is remarkably lower in the $Col17^{-/-}$ mouse (**L**) than that in the $Col17^{+/+}$ mouse (**J**). In addition, enamel rod structures are blurred in the enamel matrix of the $Col17^{-/-}$ mouse (**L**). am: ameloblast; em: enamel matrix; en: enamel; de: dentin; od: odontoblast; tp: Tomes' processes. Scale bars: (**A, C, E, G, I, K**) = 30 μm; (**B, D, F, H, J, L**) = 3 μm.

became more severe with age, although it failed to extend to loosen the molar crown (Figure 2C). In sagittal sections of the $Col17^{-/-}$ mice maxillary incisors, the enamel rod inclination was irregularly oriented and disrupted and had lost its normal network arrangement seen in that of $Col17^{+/+}$ and $Col17^{+/-}$ mice (Figure 3 A–D, F–H). In the COL17-rescued mouse $Col17^{-/-}$· human $COL17^{+/+}$ mice, the maxillary incisors showed normal enamel rod formation (Figure 3, E and I) confirming that the enamel changes were caused by a Col17 deficiency.

Chemical and Mineralization Analysis of the Teeth

Backscatter electron images of the labial surface and the sagittal sections of the maxillary incisors in the $Col17^{+/+}$, $Col17^{+/-}$, and $Col17^{-/-}$ mice revealed that calcium and phosphorus were homogeneously distributed from incisal edge to apical root in all samples (Figure 4A, B, D, E). In the $Col17^{+/+}$ and $Col17^{+/-}$ mice, iron was lightly but uniformly distributed from incisal edge to the middle of teeth, and the density corresponded with the yellow pig-

mentation. In the $Col17^{-/-}$ mice, iron was irregularly distributed (Figure 4, C and F).

To compare the mineralization patterns of teeth between the $Col17^{+/+}$ and $Col17^{-/-}$ mice, radio transparencies of the microradiographs were examined in maxillary incisors. The radio-opacity of enamel decreased gradually toward the incisal edge, from the enamel secretory stage to the maturation stage. Mineralization reached its maximum during the late maturation stage (Figure 4G). To objectively evaluate the mineralization level in the enamel layers, we set up a marker-point for enamel matrix sufficiently completed mineralization using image analysis. The point exhibited 90% or more saturation levels in the completely mineralized incisal edge-side of enamel layer. We then assessed each image for the area that showed this or higher saturation signals. The mineralization marker-points that we defined were at 1.7 mm and 2.7 mm from the incisor root in the $Col17^{+/+}$ mice and $Col17^{-/-}$ mice, respectively (Figure 4H). These findings indicated that, in the $Col17^{-/-}$ incisors, mineralization of enamel was delayed by 1.0 mm toward the incisal edge compared with that of the

$Col17^{+/+}$ incisors. Mineralization of the enamel matrix, at the maturation stage, was irregular and discontinuous in the $Col17^{-/-}$ mice (Figure 4I) compared with the $Col17^{+/+}$ mice (Figure 4J).

Defective Amelogenesis in $Col17^{-/-}$ Mice

Ameloblast size and the enamel matrix thickness in the $Col17^{-/-}$ mice were similar to those in the $Col17^{+/+}$ mice. The Tomes' processes of the $Col17^{+/+}$ mice were triangular and arranged in order. However, the processes of the $Col17^{-/-}$ mice were deformed and difficult to clearly visualize in H&E-stained sections (Figure 5A, C, E, G, I, K).

Furthermore, we observed enamel formation of the incisors of the $Col17^{+/+}$, $Col17^{+/-}$, and $Col17^{-/-}$ mice ultrastructurally. Secretory ameloblasts were tall columnar cells with intact Tomes' processes producing enamel matrix in the $Col17^{+/+}$ and $Col17^{+/-}$ mice (Figure 5, B and D).

In the $Col17^{-/-}$ mice, the Tomes' processes were thin, fragmented and disorganized, showing a wavy, villous appearance. There was no obvious difference in the other structural components of the ameloblasts (Figure 5, F and H).
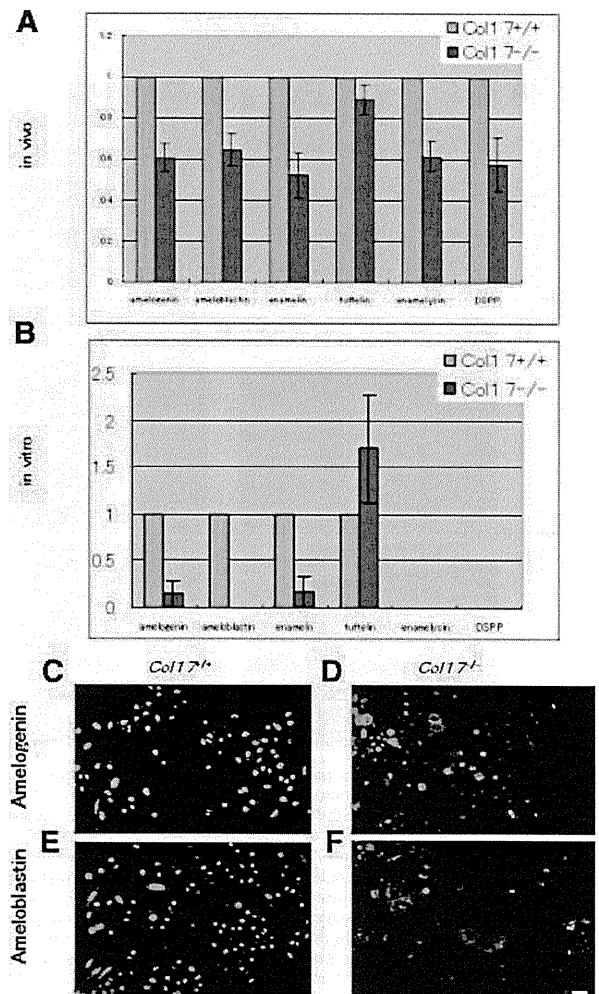
Mature ameloblasts were columnar cells and could be divided into ruffle-based ameloblasts and smooth-ended ameloblasts by the presence of a ruffled border. Rough endoplasmic reticulum, lysosomes, mitochondria, small vacuoles and Golgi apparatus were seen in the apical and mid portions of mature ameloblasts. The cell structure and organelles of $Col17^{-/-}$ mature ameloblasts appeared normal, but the enamel rods were malformed and irregularly distributed. The electron density of the enamel matrix was remarkably low during the secretory and maturation stages in the $Col17^{-/-}$ mice, compared with the high electron density of the enamel matrix in the $Col17^{+/+}$ and $Col17^{+/-}$ mice (Figure 5, J and L).

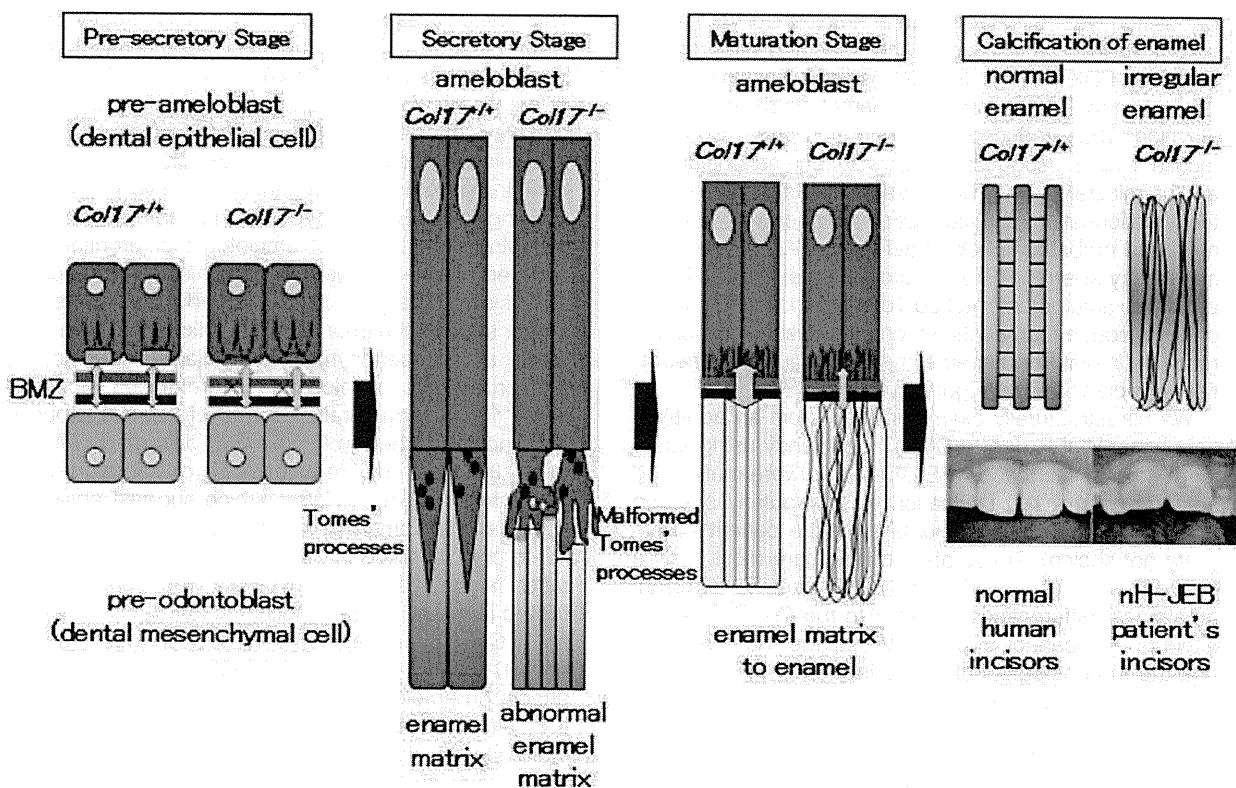## Assay of Ameloblast Proliferation and Differentiation

Colony-forming analysis revealed there was no significant difference in colony-forming ability of cultured ameloblasts between the $Col17^{+/+}$ and $Col17^{-/-}$ mice (data not shown). As for apoptosis, TUNEL staining did not reveal excessive apoptosis of ameloblasts at the pre-secretory to secretory stages in either the $Col17^{+/+}$ or the $Col17^{-/-}$ mice (data not shown).

TUNEL assays showed that some apoptotic cells appeared from the late secretory stage to the early maturation stage (called the "transitional stage") of the $Col17^{+/+}$ and $Col17^{-/-}$ mice (data not shown). However, there was no significant difference in the number of TUNEL-positive cells between $Col17^{+/+}$ and $Col17^{-/-}$ mice; in the numbers of apoptotic ameloblasts per sagittal incisor section, 7.5 ± 0.7 cells/sagittal section in $Col17^{+/+}$ incisors and 7.0 ± 1.0 cells/sagittal section in $Col17^{-/-}$ incisors.

We examined the expression of enamel proteins in the incisors *in vivo* and in cultured dental epithelial cells *in vitro* using real-time RT-PCR analysis.[12–14] mRNA expression of the major enamel proteins produced by amelo-

Figure 6. Expression of enamel proteins in $Col17^{-/-}$ ameloblasts. **A:** mRNA expression of all of the enamel proteins examined (amelogenin, ameloblastin, enamelin, tuftelin, enamelysin, and DSPP) was down-regulated in ameloblasts of incisors of the $Col17^{-/-}$ mice *in vivo*. **B:** *In vitro* ameloblasts cultured from incisors of the $Col17^{-/-}$ mice showed down-regulated mRNA expression of amelogenin, ameloblastin and enamelin, although tuftelin expression was up-regulated relative to tuftelin expression of the cultured ameloblasts from the $Col17^{+/+}$ mice. Neither enamelysin nor DSPP was expressed in ameloblasts cultured from the $Col17^{+/+}$ and $Col17^{-/-}$ mice. **C:** Protein expression (FITC, green) of amelogenin and ameloblastin was decreased in ameloblasts cultured from the $Col17^{-/-}$ mice (**D, F**), relative to that in ameloblasts cultured from the $Col17^{+/+}$ mice (**C, E**). (**C, D**) amelogenin staining; (**E, F**) ameloblastin staining; (**C, E**) cells from $Col17^{+/+}$ mice; (**D, F**) cells from $Col17^{-/-}$ mice. Scale bar = 20 μm.

blasts, including amelogenin, ameloblastin, enamelin, enamelysin, and DSPP, was significantly decreased in the $Col17^{-/-}$ incisors, except for the expression of tuftelin (Figure 6A). Tuftelin expression was only slightly reduced in $Col17^{-/-}$ mice incisors. In dental epithelial cells cultured from the $Col17^{+/+}$ mice, mRNA expression of amelogenin, ameloblastin, enamelin, and tuftelin was confirmed, although mRNA expression of enamelysin and DSPP was absent. In the $Col17^{-/-}$ mice, mRNA expression of amelogenin, ameloblastin and enamelin in cultured cells were remarkably lower than in the $Col17^{+/+}$ mice. Tuftelin expression was higher than that in the cells cultured from the $Col17^{+/+}$ mice (Figure 6B). Immunocy-

Figure 7. Schemes of normal enamel formation in $Col17^{+/+}$ mice and defective enamel formation in $Col17^{-/-}$ mice. In the $Col17^{+/+}$ incisors (left), normal enamel matrix is formed by Tomes' processes, resulting in intact enamel formation. In the $Col17^{-/-}$ incisors (right), disruptive Tomes' processes produce disturbed enamel matrix, leading to irregular enamel formation.

tologically, strong expression of amelogenin and amelo-blastin was seen in the ameloblasts cultured from the $Col17^{+/+}$ mice, although expression of both proteins was remarkably weak in cells cultured from the $Col17^{-/-}$ mice (Figure 6, C–F).

Discussion

nH-JEB is a hereditary blistering skin disease with tissue separation occurring within the lamina lucida of the epidermal basement membrane zone. nH-JEB is characterized by generalized blistering, alopecia, reduced axillary and pubic hair, dystrophic nails, and dental abnormalities.[4,15] Molecular genetic studies revealed that nH-JEB is caused by mutations in the genes encoding COL17 or laminin 332.[16] Most nH-JEB patients exhibit enamel hypoplasia, and pitting and coarsening of the tooth surface enamel.[6,7]

The present study revealed that the secretory ameloblasts of the $Col17^{-/-}$ mice lacked Tomes' processes and exhibited disturbed enamel matrix secretion, which resulted in imperfect amelogenesis demonstrated by malformed enamel rods and irregular enamel matrix (Figure 7).

Mice only have one set of dentition whereas the human disease nH-JEB affects both primary and secondary dentition. Due to these differences, the tooth abnormalities demonstrated in $Col17^{-/-}$ mice are unlikely to be patho-

physiologically relevant to the nH-JEB human disease. However, the physiological processes of enamel formation are identical both in human and mouse dentition.[17,18] Thus, we believe that the present $Col17^{-/-}$ mice are a practical and useful model in which to study nH-JEB dental abnormalities.

We studied the developmental processes of the teeth in $Col17^{-/-}$ mice. The teeth develop through the pre-secretory, secretory, and maturation stages.[19] At pre-secretory stage, hypoplasia of hemidesmosomes is the only apparent abnormality in $Col17^{-/-}$ mice teeth. In ameloblasts in the secretory stage, disturbed Tomes' process formation was observed in the $Col17^{-/-}$ mice, although enamel matrix was seen around the disrupted Tomes' processes. The Tomes' processes are known to be involved in the secretion of enamel matrix.[19]

Ameloblasts at the maturation stage showed no apparent abnormality, although the crystal structure of the enamel matrix was disturbed in the $Col17^{-/-}$ mice. Scanning electron microscopy revealed that enamel rods were malformed and irregular in the enamel matrix of the $Col17^{-/-}$ mice. These morphological abnormalities were not observed in the rescued COL17-humanized mice and thus it was confirmed that the abnormalities were direct effects of the COL17 deficiency.

Contact microradiography demonstrated that enamelization of the enamel matrix and calcification were delayed in the $Col17^{-/-}$ mice. In addition, reduced iron

deposition was revealed in the enamel of Col17^{−/−} incisors from their whitish color and scanning electron microscopy-EDX findings. Iron deposition is known to occur according to the maturation of enamel matrix and mineralization. Thus, reduced iron deposition in the Col17^{−/−} mouse incisors suggests defects in enamel maturation and/or mineralization. These results clearly indicate that tooth malformation (amelogenesis imperfecta) in Col17^{−/−} mice and probably in COL17-deficient nH-JEB patients is caused by aberrant differentiation of ameloblasts. These abnormal ameloblasts lacked Tomes' processes and secreted reduced amounts of enamel matrix irregularly, resulting in disturbed enamel matrix, irregular enamelization and calcification (Figure 7).

We ultrastructurally examined teeth from an adult patient with nH-JEB due to COL17 deficiency using scanning electron microscopy. Enamel rods were malformed and the enamel rod inclination was irregularly oriented and disrupted in the enamel layer of the patient's teeth (data not shown). These abnormalities are most likely a consequence of a lack of COL17 causing aberrant ameloblast differentiation, similar to the Col17^{−/−} mice, although we cannot completely exclude the possibility that the morphological changes in the nH-JEB patient's teeth were non-specific abnormalities caused by secondary bacterial infection, etc.

It is reported that heterozygous carriers of glycine substitutions in COL17A1 show dental abnormalities,[7,20] although such dominant negative mutations in COL17A1 fail to manifest with a blistering skin phenotype.[20] It is considered that abnormal dentition in the heterozygous carriers is a direct result of dominantly inherited glycine substitutions in COL17A1 with dominant interference between the wild-type and mutant protein causing ameloblast dysfunction and disruption of enamel deposition.[20] In addition, dental abnormalities were seen both in individuals heterozygous for a COL17A1 nonsense mutation p.Arg1226X[21] and in heterozygous carriers of a COL17A1 deletion mutation c.823delA.[7] By contrast, in the present study, Col17^{+/−} mice showed no apparent tooth abnormality, probably because the critically disruptive Col17 allele carried by the mice had no dominant negative effect against wild-type COL17 protein.

Ameloblasts cultured without interaction with mesenchymal tissue cannot differentiate sufficiently to form columnar epithelium.[22] Such insufficiently differentiated ameloblasts express tuftelin, but not other enamel proteins, including amelogenin and ameloblastin.

Ameloblasts in Col17^{−/−} mice express tuftelin to an extent similar to that of Col17^{+/+} mice, Col17^{−/−} ameloblasts express reduced amounts of amelogenin and ameloblastin. Tuftelin is known to be expressed by epithelial cells at a very early stage (the pre-secretory ameloblast stage) of odontogenesis,[23,24] although other major enamel proteins are expressed at the secretory stage.[25] Thus, the results of the present enamel protein expression study further support the idea that ameloblast differentiation from the pre-secretory stage to the secretory stage is disturbed in Col17^{−/−} mice.

In the Col17^{−/−} mice, ameloblast differentiation was retarded, resulting in malformation of Tomes' processes.

The present results in Col17^{−/−} mice clearly demonstrated that COL17, a component of the hemidesmosome involved in basement membrane adhesion, also regulates differentiation of odontogenic epithelial cells in ameloblasts and plays and essential role in enamelization.

Laminin 332 is known to be an important component of hemidesmosomes and another causative molecule underlying the JEB phenotype. Remarkable abnormalities, including disturbance of ameloblast differentiation and reduced enamel deposition, have also been reported in the incisors of laminin 332-disrupted mice.[8] These facts further support the idea that interactions between ameloblasts and mesenchymal tissue via hemidesmosomes are crucial for ameloblast differentiation and function.[26,27] Ultrastructural changes of Tomes' processes were not described in laminin 332-disrupted LAMA3^{−/−} mice. However, the reduced size of secretory ameloblasts reported in LAMA3^{−/−} mice suggest absence or hypoplasia of Tomes' processes in LAMA3^{−/−} mice, similar to that observed in Col17^{−/−} mice. During the maturation stage, tissue organization was completely disrupted in the enamel epithelium of LAMA3^{−/−} mice,[8] but not of Col17^{−/−} mice. These findings suggest that a lack of COL17 and a lack of laminin 332 have similar negative effects on ameloblast differentiation and enamel formation, although laminin 332 deficiency appears to have more severe disruptive effects on enamel epithelium, compared with COL17 deficiency.

Our results show that disruption of the Col17 gene leads to abnormal interaction between enamel epithelium and the underlying mesenchyme via the EMJ, resulting in defective ameloblast differentiation. Consequently, the Col17^{−/−} mice exhibit ameloblasts with malformed Tomes' processes and the secretion of enamel matrix was diminished at the secretary stage. At the maturation stage, the Col17^{−/−} mice show delayed calcification and reduced iron deposition in the enamel. We consider that these mechanisms contribute to the immature and irregular enamel formation seen in Col17^{−/−} mice. In conclusion, epithelial-mesenchymal interactions via the EMJ are important for tooth morphogenesis, and hemidesmosome components are thought to regulate the proliferation and differentiation of tooth forming cells including ameloblasts.

References

1. Maas R, Bei M: The genetic control of early tooth development. Crit Rev Oral Biol Med 1997, 8:4–39
2. Liu F, Chu EY, Watt B, Zhang Y, Gallant NM, Andl T, Yang SH, Lu MM, Piccolo S, Schmidt-Ullrich R, Taketo MM, Morrisey EE, Atit R, Dlugosz AA, Millar SE: Wnt/beta-catenin signaling directs multiple stages of tooth morphogenesis. Dev Biol 2008, 313:210–224

3. Borradori L, Sonnenberg A: Structure and function of hemidesmosomes: more than simple adhesion complexes. J Invest Dermatol 1999, 112:411–418
4. McGrath JA, Gatalica B, Christiano AM, Li K, Owaribe K, McMillan JR, Eady RA, Uitto J: Mutations in the 180-kD bullous pemphigoid antigen (BPAG2), a hemidesmosomal transmembrane collagen (COL17A1), in generalized atrophic benign epidermolysis bullosa. Nat Genet 1995, 11:83–86
5. Kirkham J, Robinson C, Strafford SM, Shore RC, Bonass WA, Brookes SJ, Wright JT: The chemical composition of tooth enamel in recessive dystrophic epidermolysis bullosa: significance with respect to dental caries. J Dent Res 1996, 75:1672–1678
6. Nakamura H, Sawamura D, Goto M, Nakamura H, Kida M, Ariga T, Sakiyama Y, Tomizawa K, Mitsui H, Tamaki K, Shimizu H: Analysis of the COL17A1 in non-Herlitz junctional epidermolysis bullosa and amelogenesis imperfecta. Int J Mol Med 2006, 18:333–337
7. Murrell DF, Pasmooij AM, Pas HH, Marr P, Klingberg S, Pfendner E, Uitto J, Sadowski S, Collins F, Widmer R, Jonkman MF: Retrospective diagnosis of fatal BP180-deficient non-Herlitz junctional epidermolysis bullosa suggested by immunofluorescence (IF) antigen-mapping of parental carriers bearing enamel defects. J Invest Dermatol 2007, 127:1772–1775
8. Ryan MC, Lee K, Miyashita Y, Carter WG: Targeted disruption of the LAMA3 gene in mice reveals abnormalities in survival and late stage differentiation of epithelial cells. J Cell Biol 1999, 145:1309–1323
9. Nishie W, Sawamura D, Goto M, Ito K, Shibaki A, McMillan J, Sakai K, Nakamura H, Olasz E, Yancey K, Akiyama M, Shimizu H: Humanization of autoantigen. Nat Med 2007, 13:378–383 in-90
10. Tung K, Fujita H, Yamashita Y, Takagi Y: Effect of turpentine-induced feverduring the enamel formation of rat incisor. Arch Oral Biol 2006, 51:464–470
11. Osawa M, Kenmotsu S, Masuyama T, Taniguchi K, Uchida T, Saito C, Ohshima H: Rat wct mutation induces a hypo-mineralization form of amelogenesis imperfecta and cyst formation in molar teeth. Cell Tissue Res 2007, 330:97–109
12. Fukumoto S, Kiba T, Hall B, Iehara N, Nakamura T, Longenecker G, Krebsbach PH, Nanci A, Kulkarni AB, Yamada Y: Ameloblastin is a cell adhesion molecule required for maintaining the differentiation state of ameloblasts. J Cell Biol 2004, 167:973–983
13. Fukumoto S, Yamada A, Nonaka K, Yamada Y: Essential roles of ameloblastin in maintaining ameloblast differentiation and enamel formation. Cells Tissues Organs 2005, 181:189–195
14. Masuya H, Shimizu K, Sezutsu H, Sakuraba Y, Nagano J, Shimizu A, Fujimoto N, Kawai A, Miura I, Kaneda H, Kobayashi K, Ishijima J, Maeda T, Gondo Y, Noda T, Wakana S, Shiroishi T: Enamelin (Enam) is essential for amelogenesis: eNU-induced mouse mutants as mod-
els for different clinical subtypes of human amelogenesis imperfecta (AI). Hum Mol Genet 2005, 14:575–583
15. Jonkman MF, de Jong MC, Heeres K, Pas HH, van der Meer JB, Owaribe K, Martinez de Velasco AM, Niessen CM, Sonnenberg A: 180-kD bullous pemphigoid antigen (BP180) is deficient in generalized atrophic benign epidermolysis bullosa. J Clin Invest 1995, 95:1345–1352
16. Varki R, Sadowski S, Pfendner E, Uitto J: Epidermolysis bullosa. I. Molecular genetics of the junctional and hemidesmosomal variants. J Med Genet 2006, 43:641–652
17. Miletich I, Sharpe PT: Normal and abnormal dental development. Hum Mol Genet 2003, 12:R69–R73
18. Fleischmannova J, Matalova E, Tucker AS, Sharpe PT: Mouse models of tooth abnormalities. Eur J Oral Sci 2008, 116:1–10
19. Smith CE: Cellular and chemical events during enamel maturation. Crit Rev Oral Biol Med 1998, 9:128–161
20. McGrath JA, Gatalica B, Li K, Dunnill MG, McMillan JR, Christiano AM, Eady RA, Uitto J: Compound heterozygosity for a dominant glycine substitution and a recessive internal duplication mutation in the type XVII collagen gene results in junctional epidermolysis bullosa and abnormal dentition. Am J Pathol 1996, 148:1787–1796
21. Floeth M, Bruckner-Tuderman L: Digenic junctional epidermolysis bullosa: mutations in COL17A1 and LAMB3 genes. Am J Hum Genet 1999, 65:1530–1537
22. Morotomi T, Kawano S, Toyono T, Kitamura C, Terashita M, Uchida T, Toyoshima K, Harada H: In vitro differentiation of dental epithelial progenitor cells through epithelial-mesenchymal interactions. Arch Oral Biol 2005, 50:695–705
23. Deutsch D, Leiser Y, Shay B, Fermon E, Taylor A, Rosenfeld E, Dafni L, Charuvi K, Cohen Y, Haze A, Fuks A, Mao Z: The human tuftelin gene and the expression of tuftelin in mineralizing and nonmineralizing tissues. Connect Tissue Res 2002, 43:425–434
24. Leiser Y, Blumenfeld A, Haze A, Dafni L, Taylor AL, Rosenfeld E, Fermon E, Gruenbaum-Cohen Y, Shay B, Deutsch D: Localization, quantification, and characterization of tuftelin in soft tissues. Anat Rec 2007, 290:449–454
25. Fukumoto S, Yamada Y: Extracellular matrix regulates tooth morphogenesis. Connect Tissue Res 2005, 46:220–226
26. Yoshiba K, Yoshiba N, Aberdam D, Meneguzzi G, Perrin-Schmitt F, Stoetzel C, Ruch JV and Lesot H: Expression and localization of laminin-5 subunits during mouse tooth development. Dev Dyn 1998, 211:164–176
27. Fukumoto S, Miner JH, Ida H, Fukumoto E, Yuasa K, Miyazaki H, Hoffman MP, Yamada Y: Laminin alpha5 is required for dental epithelium growth and polarity and the development of tooth bud and shape. J Biol Chem 2006, 24;281:5008–5016

Letter to the Editor

A novel *OSMR* mutation in familial primary localized cutaneous amyloidosis in a Japanese family

To the Editor,

Primary localized cutaneous amyloidosis (PLCA) is a pruritic skin disorder in which there is deposition of amyloid material in the papillary dermis. Clinically, skin lesions comprise small, flat-top papules (lichen amyloidosis) or brown-gray macules (macular amyloidosis). Organs other than skin are not involved. The "amyloid" in PLCA probably represents a combination of degenerate keratin filaments from apoptotic basal keratinocytes, and deposition of serum amyloid P component and immunoglobulins [1,2]. PLCA is relatively common in South America and Asia, and some cases have an autosomal dominant family history (familial PLCA, FPLCA) [MIM 105250].

The genetic basis of FPLCA has been shown to involve mutations in the *OSMR* gene, which encodes the oncostatin M receptor β subunit (OSMRβ) [3]. OSMRβ is one of the interleukin-6 type cytokine receptors [4]. The ligands are oncostatin M (OSM) and interleukin-31 (IL-31), which both have biologic roles linked to keratinocyte cell proliferation, differentiation, apoptosis and inflammation [5–7]. Thus far, only two pathogenic mutations in *OSMR* in cases of FPLCA have been published [3]. We now report a Japanese family with FPLCA in whom a further, novel *OSMR* mutation was observed.

The proband is a 29-year-old Japanese female. She had suffered from chronic itching for 7 years. Her mother and a maternal cousin have similar symptoms. On examination, numerous dusky erythematous or brown, flat-top papules up to 2 mm in diameter were noted on her trunk and extremities (Fig. 1a). Skin biopsy revealed focal collections of amorphous eosinophilic material in the papillary dermis (Fig. 1b), which stained positively with Direct Fast Scarlet (Fig. 1c). These findings support a clinico-pathologic diagnosis of lichen amyloidosis.

Following informed consent, DNA was extracted from peripheral blood samples obtained from the proband and her mother. For sequencing, DNA samples were amplified with primers sited in introns flanking individual exons of the *OSMR* gene as described previously [3]. Sequencing showed a heterozygous missense mutation, c.2168G > T, p.G723V (NM_003999) in exon 15, in DNA samples from both the proband and her mother (Fig. 2a). The mutation was further confirmed by enzyme digestion using *NlaIV* (Fig. 2b) and was not observed in screening 200 ethically matched control chromosomes. The amino acid G723 is well conserved in other interleukin-6 type cytokine receptors (including interleukin-31RA, leukemia inhibitory factor receptor and interleukin-6 signal transducer), and also in other mammalian species (including mouse and rat).

The *OSMR* mutation p.G723V is located within the first fibronectin type III (FNIII)-like domain adjacent to the transmembranous domain (Fig. 2c). The nature and site of this mutation is similar to the previously reported mutations, p.I691T and p.G618A, which are also within the FNIII-like domains [3]. Previous studies have disclosed important roles for the FNIII-

like domains in receptor dimerization, a key event in cytokine signaling [8,9]. Of note, in keratinocytes harboring the heterozygous mutation p.G618A there is reduced phosphorylation of STATs, ERKs and Akt following stimulation by OSM or IL-31, consistent with a functional disruption of OSMRβ [3]. The new mutation p.G723V underscores the functional importance of FNIII-like domains in this cytokine receptor and in the pathogenesis of FPLCA.

The exact pathomechanism of how the mutations in OSMRβ lead to clinical phenotype of PLCA has yet to be clarified. However, the reason why the mutations result in what is predominantly a skin disease may be explained as the keratinocytes do not express leukemia inhibitory factor receptor, which is another receptor of OSM and may compensate the abnormal function of OSMRβ [7]. OSM has various effects for keratinocyte biology, including proliferation, differentiation, apoptosis and inflammation. For example, both OSM and
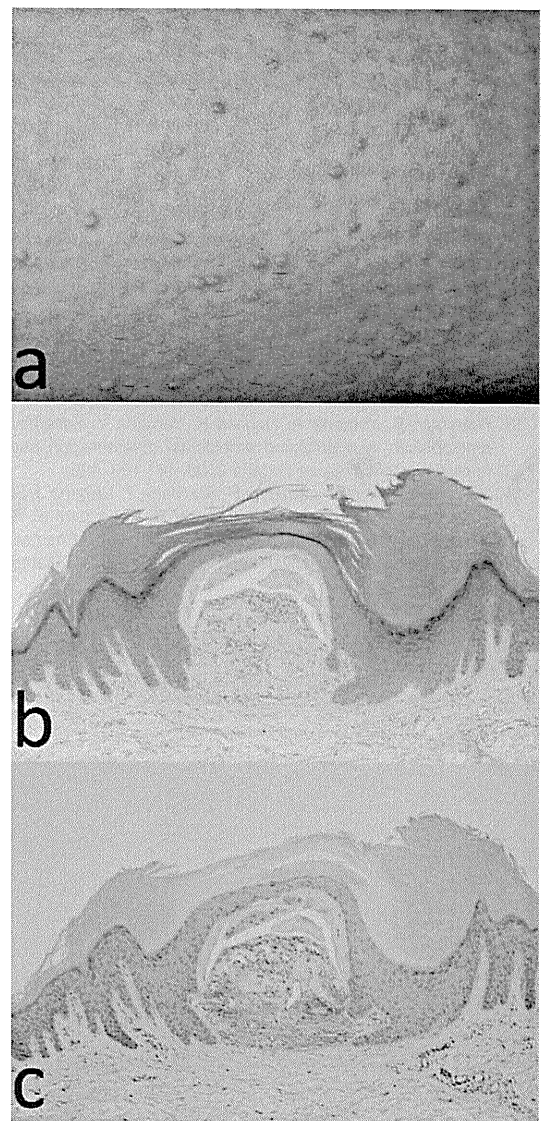
Fig. 1. Clinical and histologic features of FPLCA. (a) There are flat-top, brownish papules up to 2 mm across the proband's left arm. (b) Light microscopy of lesional skin shows a collection of amorphous material within the papillary dermis. (c) This material stains positively with Direct Fast Scarlet.
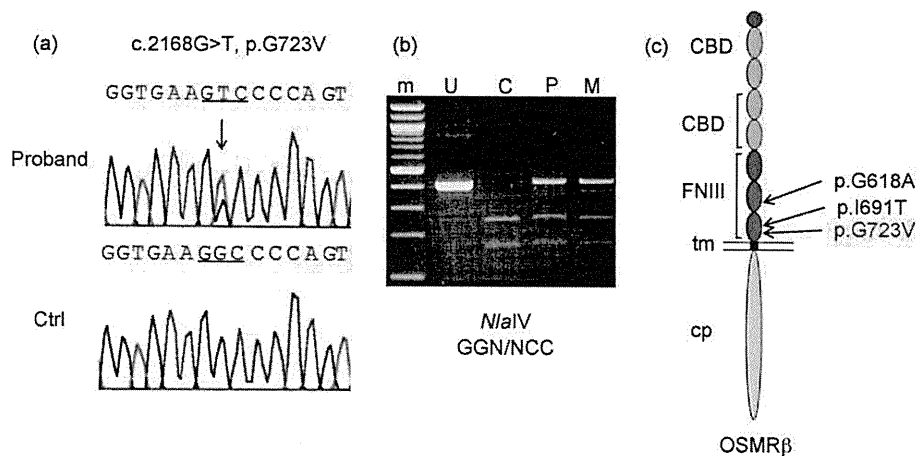
Fig. 2. FPLCA in this family results from the mutation p.G723V in the oncostatin M receptor β. (a) A heterozygous nucleotide substitution, c.2168G > T (NM_003999) in the OSMR gene is present in the proband and her mother. (b) The mutation abolishes a restriction enzyme cut site for NlaIV, resulting in an undigested DNA band in affected individuals. M, marker; U, control (undigested); C, control (digested); P, proband; M, proband's mother. (Digested PCR product spans exon 15 and flanking introns of OSMR.) (c) The mutation p.G723V is located within the FNIII-like domain region, similarly to the previous reported mutations, p.G618A and p.I691T. CBD, cytokine binding domain; FNIII, fibronectin type III-like domain; tm, transmembranous domain; cp, cytoplasmic domain.

OSMRβ were upregulated in psoriatic and atopic skin, suggesting that OSM is a potent activator of skin inflammation [7]. As to PLCA, the histopathological finding of inflammation is less obvious, and main histological features are the pigmentary incontinence and amyloids in the papillary dermis suggesting the apoptosis of basal keratinocytes. Jak/STAT, Erk1/2 and PI3K/Akt signaling, which is downstream of IL-6 type cytokine signaling, have been reported to have antiapoptotic effects in several tumor cell lines [10,11]. These findings suggest the functional decrease of IL-6 type cytokine receptor (including OSMRβ) may lead to a condition that is more susceptible to apoptosis. Recently, diminished innervations of epidermis and dermoepidermal junction were identified in PLCA skin, indicating the damage to the nerve fibers as a possible explanation for the severe pruritis [12]. It is speculated that the pruritis may be the result of hypersensitivity of the remaining nerve fibers as a response to the neurodegeneration [12]. OSMRβ is also expressed in afferent nerve fibers in the spinal cord and the dermis of the skin [13]; therefore, the pathophysiology of PLCA may involve both cutaneous and neural components.

Although FPLCA is relatively common in Asian countries, our case represents the first OSMR mutation to be reported in Japanese population.

References

[1] Kumakiri M, Hashimoto K. Histogenesis of primary localized cutaneous amyloidosis: sequential change of epidermal keratinocytes to amyloid via filamentous degeneration. J Invest Dermatol 1979;73:150–62.

[2] Kobayashi H, Hashimoto K. Amyloidogenesis in organ-limited cutaneous amyloidosis: an antigenic identity between epidermal keratin and skin amyloid. J Invest Dermatol 1983;80:66–72.

[3] Arita K, South AP, Hans-Filho G, Sakuma TH, Lai-Cheong J, Clements S, et al. Oncostatin M receptor-beta mutations underlie familial primary localized cutaneous amyloidosis. Am J Hum Genet 2008;82:73–80.

[4] Heinrich PC, Behrmann I, Haan S, Hermanns HM, Muller-Newen G, Schaper F. Principles of interleukin (IL)-6-type cytokine signalling and its regulation. Biochem J 2003;374:1–20.

[5] Dillon SR, Sprecher C, Hammond A, Bilsborough J, Rosenfeld-Franklin M, Presnell SR, et al. Interleukin 31, a cytokine produced by activated T cells, induces dermatitis in mice. Nat Immunol 2004;5:752–60.

[6] Finelt N, Gazel A, Gorelick S, Blumenberg M. Transcriptional responses of human epidermal keratinocytes to oncostatin-M. Cytokine 2005;31:305–13.

[7] Boniface K, Diveu C, Morel F, Pedretti N, Froger J, Ravon E, et al. Oncostatin M secreted by skin infiltrating T lymphocytes is a potent keratinocyte activator involved in skin inflammation. J Immunol 2007;178:4615–22.

[8] Kurth I, Horsten U, Pflanz S, Timmermann A, Kuster A, Dahmen H, et al. Importance of the membrane-proximal extracellular domains for activation of the signal transducer glycoprotein 130. J Immunol 2000;164:273–82.

[9] Timmermann A, Küster A, Kurth I, Heinrich PC, Müller-Newen G. A functional role of the membrane-proximal extracellular domains of the signal transducer gp130 in heterodimerization with the leukemia inhibitory factor receptor. Eur J Biochem 2002;269:2716–26.

[10] Chen RH, Chang MC, Su YH, Tsai YH, Kuo ML. Interleukin-6 inhibits transforming growth factor beta-induced apoptosis through the phosphatidylinositol 3-kinase/Akt and signal transducers and activators of transcription 3 pathways. J Biol Chem 1999;274:23013–9.

[11] Mirmohammadsadegh A, Mota R, Gustrau A, Hassan M, Nambiar S, Marini A, et al. ERK1/2 is highly phosphorylated in melanoma metastases and protects melanoma cells from cisplatin-mediated apoptosis. J Invest Dermatol 2007;127:2207–15.

[12] Maddison B, Namazi MR, Samuel LS, Sanchez J, Pichardo R, Stocks J, et al. Unexpected diminished innervation of epidermis and dermoepidermal junction in lichen amyloidosis. Br J Dermatol 2008;159:403–6.

[13] Bando T, Morikawa Y, Komori T, Senba E. Complete overlap of interleukin 31 receptor A and oncostatin M receptor beta in the adult dorsal root ganglia with distinct developmental expression pattern. Neuroscience 2006;142:1263–71.

Ken Arita[a,*]
Riichiro Abe[a]
Keiko Baba[a]
John A. McGrath[b]
Masashi Akiyama[a]
Hiroshi Shimizu[a]

[a]Department of Dermatology, Hokkaido University Graduate School of Medicine, North 15 West 7, Kita-ku, Sapporo 060-8638, Japan
[b]Genetic Skin Disease Group, St. John's Institute of Dermatology, Division of Genetics and Molecular Medicine, King's College London (Guy's Campus), London, UK

*Corresponding author. Tel.: +81 11 706 7387; fax: +81 11 706 7820
E-mail address: ariken@med.hokudai.ac.jp (K. Arita)

9 January 2009

Usefulness of real-time tissue elastography for detecting lymph-node metastases in squamous cell carcinoma

S. Aoyagi, K. Izumi, H. Hata, H. Kawasaki and H. Shimizu

Department of Dermatology, Hokkaido University Graduate School of Medicine, Sapporo, Japan

Summary

We report a case of invasive SCC arising from multiple lesions of Bowen's disease with right inguinal lymph-node metastasis. Assessment of superficial lymph-node involvement by real-time tissue elastography before surgery was found to be more useful than other noninvasive conventional methods. Histologically, the metastatic tumour cells were located asymmetrically in a small section of the cortical area of the right node, and this result was comparable with the elastographic findings. Additionally, we found that the presence of an asymmetrical cortical area with high elasticity should be included in the determination of metastatic involvement in small lymph nodes. It has high predictive values in the differentiation of benign and malignant superficial lymph nodes in patients with clinically node-negative skin cancer. More cases are needed to validate this efficiency in differentiating benign from malignant lymph-node status, but if confirmed, it may have an important role in the diagnosis of high-risk cutaneous squamous cell carcinoma.

Assessment of superficial lymph-node involvement in patients with cutaneous malignancies before surgery is often difficult. In the inguinal lymph node particularly, swelling from secondary inflammation is often seen in carcinoma arising from the leg. It would be beneficial if differentiation between reactive and metastatic lymph nodes could be made through noninvasive methods. We report the novel use of real-time tissue elastography for the assessment of lymph-node involvement in a patient with invasive squamous cell carcinoma (SCC), and discuss the potential advantages of this technology over other diagnostic techniques.

Report

An 80-year-old Japanese woman presented with a 15-year history of an asymptomatic keratotic plaque on her

Correspondence: Dr Satoru Aoyagi, Department of Dermatology, Hokkaido University Graduate School of Medicine, N15 W7, Kita-ku, Sapporo 060-8638, Japan
E-mail: saoyagi@med.hokudai.ac.jp

Conflict of interest: none declared.

right lower leg. The lesion had been gradually enlarging, and new small lesions had been arising on her right dorsal foot, thigh and left leg over several months. There was no history of immunosuppression, arsenic exposure or internal malignancy.

On physical examination, a large, red to dark-brown, keratotic plaque measuring 100 mm in diameter was seen on the right pretibial site of the lower leg, with similar multiple small scaly plaques, up to 20 mm in diameter, on both legs (Fig. 1a). The central area of the plaque in the main lesion was markedly raised, with thickened scales and crusting (Fig. 1b). Although there was regional lymphadenopathy in both groins, the clinical appearance suggested secondary inflammation from the regional area, because the nodes felt soft and flat.

A punch biopsy was taken from the large plaque on the right lower leg. The initial histological examination found an intraepidermal neoplasm of atypical keratinocytes characterized by dyskeratotic and mitotic cells. There was no evidence of dermal invasion by tumour cells, indicating a diagnosis of Bowen's disease. Additionally, no evidence of metastasis was found in a computed tomography scan of the whole body including regional lymph nodes at the time of presentation.
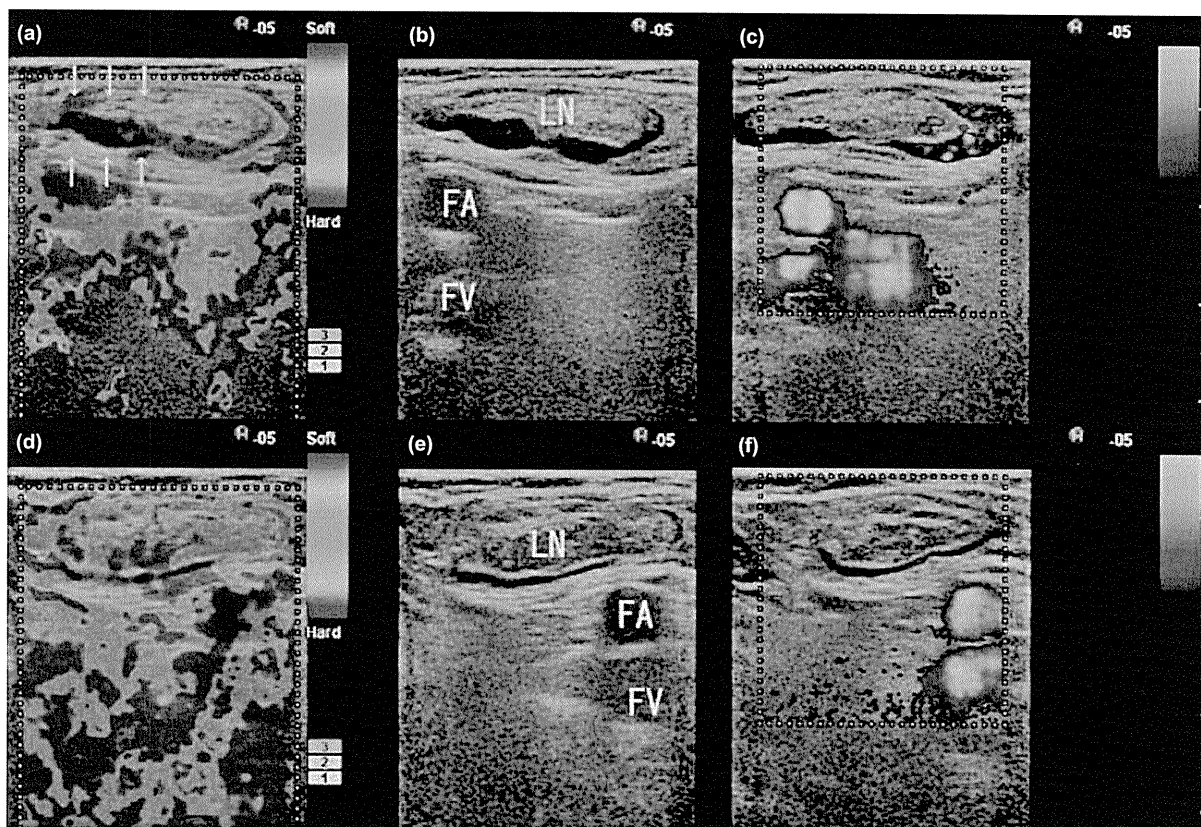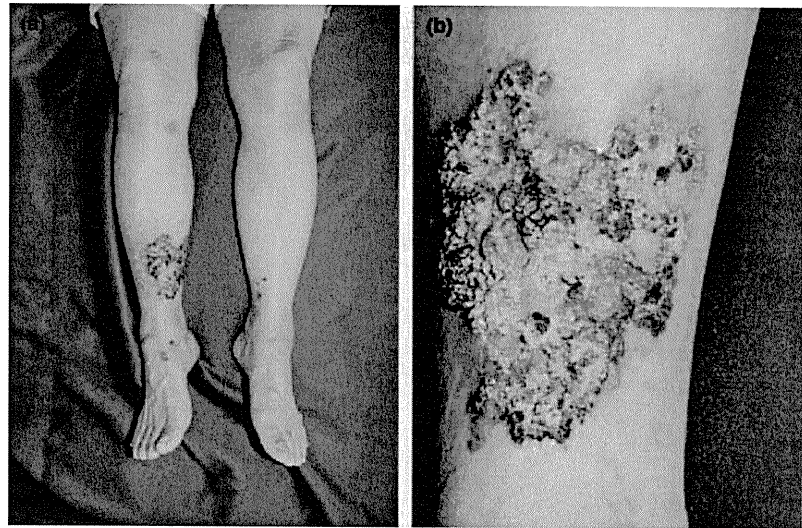
Figure 1 (a) Large, red to dark-brown keratotic plaque measuring 100 mm in diameter on the right pretibial area, with similar multiple small scaly plaques, up to 20 mm in diameter, on both legs; (b) the central area of the lesion on the right pretibial area was markedly raised by thickened scale and crust.

Figure 2 (a–c) Right inguinal lymph node visualized by (a) elastography, showing asymmetrical areas of high elasticity appearing as deep blue in the cortical area (arrows); (b) B-mode sonography; and (c) power Doppler sonography, showing presence of peripheral flow. (d,e) Left inguinal lymph node visualized by (d) elastography, showing several small areas of high elasticity appearing as blue; (e) B-mode sonography; (f) power Doppler sonography, showing weak central hilar and perihilar flow. FA, femoral artery; FV, femoral vein; LN, lymph node.

e745
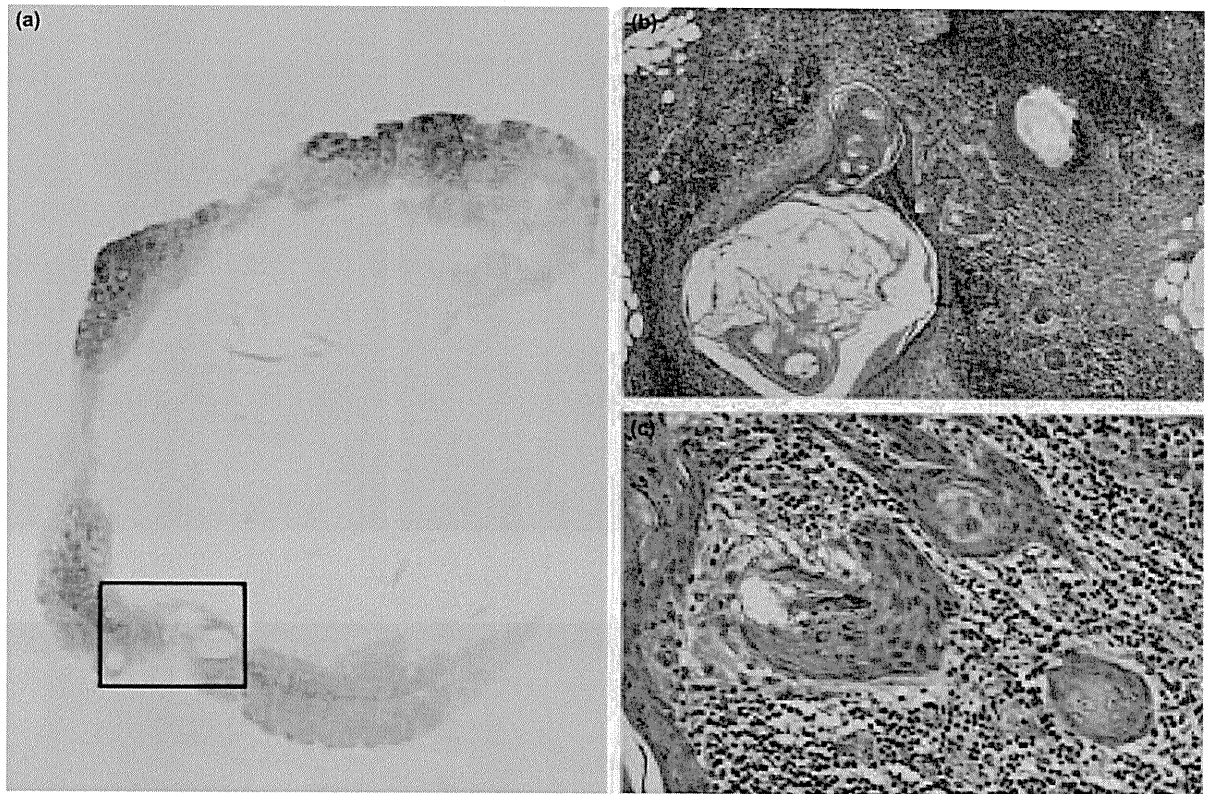
Figure 3 (a) Metastatic area located in a small section of the cortical area, with (b) replacement of the fatty tissue in the centre of the node. (c) Keratinizing squamous differentiation and cell atypia. Haematoxylin and eosin, original magnification (b) × 100 (c) × 200.

The patient underwent ultrasonography (US) examination with a digital sonography scanner (HI VISION 900; Hitachi Medical Corp., Tokyo, Japan) equipped with real-time tissue elastography software (Hitachi Medical). Presence of peripheral flow was seen on Doppler US and an asymmetrical cortical area with high elasticity (appearing as deep blue) on the real-time tissue elastography scan (Fig. 2a–c). These findings were detected only for the right and not the left inguinal lymph node (Fig. 2d–f).

The lesion was excised widely including the underlying fascia and a bilateral inguinal lymph-node biopsy was taken. The surgical specimen showed neoplastic proliferation of differentiated squamous tumour cells with dyskeratotic and atypical keratinocytes throughout the epidermis and into the dermis. The nuclei of the atypical cells were large, pleomorphic and hyperchromatic, with aberrant mitotic nuclei. Invasion of tumour cells into the dermis was seen only in the centre of the lesion. Histological examination of the inguinal lymph-node biopsies confirmed the presence of metastatic tumour cells

located asymmetrically in a small section of the cortical area in the right node only (Fig. 3). The left inguinal node was histopathologically confirmed as reactive enlargement.

The final diagnosis of invasive SCC arising from multiple Bowen's disease with right inguinal lymph-node metastasis was made. Because of the right inguinal lymph-node involvement, lymph-node dissection was added to the treatment. The patient was free of disease 4 months after surgery with no recurrence or metastasis.

The development of easy and objective noninvasive methods for the assessment of superficial lymph-node metastasis from cutaneous malignancies would be beneficial in cancer treatment. In evaluating lymph-node metastases, US has several advantages over other conventional imaging methods such as computed tomography, magnetic resonance imaging, scintigraphy and positron emission tomography.[1–3] The characteristic findings for lymph-node metastasis are a low longitudinal and transverse axis ratio (indicating that the shape of the node is round), absence of echogenic

hilum, asymmetrical cortical thickening on usual B-mode US scans, and presence of peripheral flow on Doppler US.[1] However none of these findings is sufficient to replace histopathological examination.

Elasticity is one of the differentiating criteria for metastatic and reactive lymph nodes.[4] In accordance with the hypothesis that solid tumour cells differ in their consistency from adjacent normal tissue,[5] real-time elastography is a new technology for measuring tissue elasticity, using US.[6] It visualizes the differences in tissue strain produced by freehand compression, with tissue appearing on the elastogram as red, yellow, green and blue in ascending order of tissue hardness. Diagnostic use of tissue elastography in breast cancer,[7] thyroid tumour,[8] and lymph-node enlargement in head and neck cancers[9] has already been reported, but to our knowledge, there has been no previous report of diagnostic evaluation of lymph nodes in cases of cutaneous SCC.

According to the previous literature, elastographic patterns are determined by the distribution and percentage of the lymph-node area, with increased tissue hardness appearing as blue areas.[9] The elastographic pattern of our patient shows the blue area corresponding to a reactive node, consistent with this evaluation system (blue area < 45%). The metastatic area was located in a small section of the cortical area and the loss of fatty tissue was seen in the centre of the node, therefore, the lymph node presented as a flattened ring-shaped lesion with an asymmetrical cortical area, with high elasticity appearing as blue and the central low elasticity appearing as red on the elastogram. This finding was not seen in the contralateral inguinal lymph node, which was histopathologically confirmed as a reactive enlargement. Therefore, we suggest that the presence of an asymmetrical cortical area with high elasticity should be included in the elastographic pattern evaluation system for the determination of metastatic involvement in small lymph nodes.

Currently, preoperative determination of metastatic involvement in nonpalpable or small lymph nodes from cutaneous SCC is difficult, and it is still unclear whether surgeons should carry out a lymph-node biopsy or proceed directly to lymph-node dissection. Real-time tissue elastography is a noninvasive and convenient method, especially when combined with Doppler US, which could increase the accuracy of evaluation of metastatic lymph nodes, thus eliminating unnecessary lymph-node biopsy. It also has the potential to detect early metastasis. Further studies are warranted to confirm the usefulness of this technique in tumour evaluation.

References

1 Esen G, Gurses B, Yilmaz MH. Gray scale and power Doppler US in the preoperative evaluation of axillary metastases in breast cancer patients with no palpable lymph nodes. *Eur Radiol* 2005; **15**: 1215–23.

2 Ueda S, Tsuda H, Asakawa H *et al.* Utility of 18F-fluoro-deoxyglucose emission tomography/computed tomography fusion imaging (18F-FDG PET/CT) in combination with ultrasonography for axillary staging in primary breast cancer. *BMC Cancer* 2008; **8**: 165.

3 Sato K, Tamaki K, Tsuda H *et al.* Utility of axillary ultrasound examination to select breast cancer patients suited for optimal sentinel node biopsy. *Am J Surg* 2004; **187**: 679–83.

4 Ueno E, Tohno E, Soeda S *et al.* Dynamic tests in real-time breast echography. *Ultrasound Med Biol* 1988; **14** (Suppl. 1): 53–7.

5 Krouskop TA, Wheeler TM, Kallel F *et al.* Elastic moduli of breast and prostate tissues under compression. *Ultrason Imaging* 1998; **20**: 260–74.

6 Ophir J, Céspedes I, Ponnekanti H *et al.* Elastography. A quantitative method for imaging the elasticity of biological tissues. *Ultrason Imaging* 1991; **13**: 111–34.

7 Thomas A, Fischer T, Frey H *et al.* Real-time elastography – an advanced method of ultrasound: first results in 108 patients with breast lesions. *Ultrasound Obstet Gynecol* 2006; **28**: 335–40.

8 Asteria C, Giovanardi A, Pizzocaro A *et al.* US-elastography in the differential diagnosis of benign and malignant thyroid nodules. *Thyroid* 2008; **18**: 523–31.

9 Alam F, Naito K, Horiguchi J *et al.* Accuracy of sonographic elastography in the differential diagnosis of enlarged cervical lymph nodes: comparison with conventional B-mode sonography. *AJR Am J Roentgenol* 2008; **191**: 604–10.

Journal of
Cutaneous Pathology

Letter to the Editor

Squamous cell carcinoma of the auricle with rhabdoid features

To the Editor,

Squamous cell carcinoma (SCC) is one of the most common malignancies of the external ear. It frequently occurs in elderly people and is associated with a higher metastasis rate, compared to carcinoma found in other locations.[1] As prognoses differ significantly among cutaneous SCC variants,[2] histopathological patterns of individual cases must be carefully examined.

Cutaneous SCC can be classified into several histologic subtypes, differing in prognostic significance.[2] A low-risk subtype includes verrucous SCC and those arising in actinic keratosis. An intermediate-risk subtype consists of adenoid SCC and lymphoepithelioma-like carcinoma. Finally, SCC arising from scars, Bowen's disease with invasion and adenosquamous carcinoma constitute a high-risk subtype. Other rare subtypes, of which a prognosis is not well established, include signet ring cell SCC, follicular SCC, papillary SCC, pigmented SCC, and clear cell SCC. Further studies are required to define the biological behavior and establish a prognostic indication of these rare subtypes of SCC.

Cutaneous SCC with a rhabdoid phenotype is histologically characterized by large cytoplasmic eosinophilic hyaline inclusions with peripheral displacement of vesicular nuclei. Immunohistochemically, these tumor cells show diffused reactivity for cytokeratin and vimentin, which are localized to the cytoplasmic inclusions, but usually not for desmin, smooth muscle actin, or other skeletal muscle markers. To the best of our knowledge, only a few cases of cutaneous SCC with such rhabdoid features have been reported in the literature.[3–6]

An 88-year-old Japanese man presented with an ulcerated reddish colored tumor on the right ear. The tumor, which initially appeared as a small, crusted nodule 2 years ago, had slowly enlarged in size. Bleeding had been occurring from the surface of the tumor for the past 6 months. The past medical history indicates that the patient had been diagnosed with a cerebral infarction and dementia for

3 years. The patient has been taking an anticoagulant agent without any immunosuppressive drug. Physical examination revealed an erosive, fresh-reddish colored, 37 × 25 × 14–mm sized nodule on the right post-auricular shaded area (Fig. 1A). No evidence of regional lymphadenopathy was reported at the time of presentation.

The histological examination of an incision biopsy initially led to the diagnosis of pyogenic granuloma with fibrosis. However, as the small biopsy specimen was taken from a relatively shallow region, the possibility that the nodule represented a case of undifferentiated SCC, could not be completely excluded. Therefore, the lesion was excised widely including cartilage to test for possible malignancy.

The surgical specimen showed dense, dermal and subcutaneous neoplastic proliferation (Fig. 1B) of poorly differentiated tumor cells with numerous plasma cells and histiocytes. The tumor cells consisted predominantly of monomorphic polygonal neoplastic cells, arranged in focally solid sheets (Fig. 2A), particularly in the center of the nodule. The cells possessed abundant eosinophilic, cytoplasmic inclusions with peripheral displacement of the nuclei, charactereristic of the rhabdoid phenotype (Fig. 2B). Vascular invasion and lymphatic permeation were not observed. Actinic keratosis in the overlying epidermis was identified only at the border of the nodule as the epidermis was extensively ulcerated.

The tumor cells were tested positive for vimentin and cytokeratin AE1/AE3, but negative for S-100, desmin or smooth muscle actin (SMA). Interestingly, the area tested positive for cytokeratin AE1/AE3 was localized only to the center portion of the lesion (Fig. 2C).

One year after his surgery, the patient remains alive and has not developed any metastatic or recurrent lesions.

Since malignant rhabdoid tumor of the kidney was first described,[7] additional, extra-renal cases have been reported. These cases were regarded as a variant of rhabdomyosarcomatous tumor, based on

919